Master thesis
修士論文

Improvement of timing performance of the WAGASCI neutrino detector
(ニュートリノ検出器 WAGASCI の時間測定性能の改善)

January 30th, 2020

Department of Physics, Graduate School of Science,
The University of Tokyo
東京大学大学院理学系研究科物理学専攻

Kohei Matsushita
松下 昂平

Abstract

In order to reduce systematic errors on the T2K neutrino oscillation measurement, we study the neutrino-nucleus interaction at around 1 GeV by measuring the charged-current neutrino cross section ratio between H_2O and CH with a large phase space in the T2K-WAGASCI project. We have developed a neutrino detector named WAGASCI which enables the measurement of cross section on H_2O. Precise measurements are realized by the combination with a muon range detector(MRD) named WallMRD which tracks secondary particles from neutrino interactions.

As a preparation for the physics run, a mass test of the frontend board for a WAGASCI detector was conducted at the University of Tokyo in April 2019. We checked performances for the MPPC gain tuning and the threshold curve measurement. In addition, we measured the TDC functions for each frontend board to calibrate the difference.

In order to solve a problem with a timing measurement found in the previous run, we improved an electronics firmware. The updated firmware synchronized the timing measurement system to the T2K neutrino beam timing.

We started the first physics run with two WAGASCI detectors and two WallMRD detectors in November 2019. We calibrated the timing measurement system of the WAGASCI detector using the beam data. The difference between the frontend boards and timing jitters were calibrated. The calibration improved the timing resolution of the WAGASCI detector from 15ns to 6.0ns.

A performance with timing information was evaluated using a Monte Carlo simulation. Background events from outside of the WAGASCI detector are rejected using the hit timings of WAGASCI and WallMRD. A developed method for the background event rejection has shown a potential to suppress the background under 10 % of the signal event even though the number of the background event is 4 times larger than that of the signal event.

Contents

Chapter 1

T2K experiment

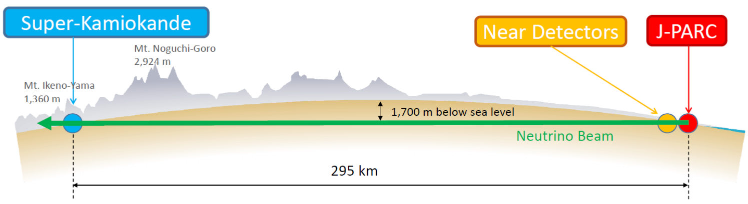

Figure 1.1: Schematic view of the T2K experiment

T2K(Tokai-to-Kamioka) is a long baseline neutrino oscillation experiment. T2K's goal is to measure the neutrino oscillation parameters and the neutrino CP violation. T2K measures muon neutrino disappearance and electron neutrino appearance in accelerator-produced neutrino and anti-neutrino beams. A schematic view of the T2K experiment is shown in Figure 1.1. An intense muon (anti-)neutrino beam is produced at the Japan Proton Accelerator Reserch Complex(J-PARC) in Tokai village, Ibaraki prefecture, on the east coast of Japan. The beam is monitored by a detector complex in Tokai, 280 m away from the neutrino target. It is aimed at the Super-Kamiokande in Kamioka, Gifu prefecture, 295 km away from Tokai. The physics motivation and the details of the T2K experiment are explained in this chapter.

1.1 Physics motivation

Our understanding of the laws of the nature is embodied in the Standard Model of particles physics, which provides a unified picture where the interactions between paticles are themselves described by the exchange of particles. The Standard Model provides a successful description of almost all experimental data and represents one of the triumphs of modern physics. However, there are unsolved problems in particle physics which cannot be explained by the current Standard Model. In order to develop a new theory beyond the Standard Model which answer the problems, there have been many theoretical and experimental approaches. Neutrino experiment is one of them. Neutrinos are a kind of elementary particles and the neutral particles with spin 1/2. Neutrinos interact only via weak interaction. Therefore neutrinos are not directly observed unlike the charged particles. That is why it took much time to discover the exsistence of neutrinos. After the discovery, neutrinos have been studied around the world.

1.1.1 Neutrino oscillation

Neutrinos have three different flavors, electron-neutrino(ν_e), muon-neutrino(ν_μ) and tau-neutrino(ν_τ). Different neutrino flavors are distinguished by the flavors of the charged lepton produced in charged-current weak interactions. Neutrinos undergo flavor transitions as they propagate over large distances. The phenomenon is referred to as "Neutrino oscillation". Neutrino oscillations are quantum-mechanical phenomena and can be described in terms of the relationship between the eigenstates of the weak interaction ν_e, ν_μ, and ν_τ, and the eigenstates of the free-paticle Hamiltonian, known as the mass eigenstates, ν_1, ν_2 and ν_3. The basis of weak enginstates can be related to the basis of mass eigenstates by the 3×3 unitary Pontecorvo-Maki-Nakagawa-Sakata(PMNS) matrix,

$$\begin{pmatrix} \nu_e \\ \nu_\mu \\ \nu_\tau \end{pmatrix} = \begin{pmatrix} U_{e1} & U_{e2} & U_{e3} \\ U_{\mu 1} & U_{\mu 2} & U_{\mu 3} \\ U_{\tau 1} & U_{\tau 2} & U_{\tau 3} \end{pmatrix} \begin{pmatrix} \nu_1 \\ \nu_2 \\ \nu_3 \end{pmatrix} \tag{1.1}$$

In the standard three-flavor mixing, the PMNS matrix can be described in terms of three mixing angles, θ_{12}, θ_{23} amd θ_{13} parameters and a CP violation phase, δ_{CP}.

$$\begin{aligned} U_{PMNS} &= \begin{pmatrix} 1 & 0 & 0 \\ 0 & c_{23} & s_{23} \\ 0 & -s_{23} & c_{23} \end{pmatrix} \begin{pmatrix} c_{13} & 0 & s_{13}e^{-i\delta_{CP}} \\ 0 & 1 & 0 \\ -s_{13}e^{i\delta_{CP}} & 0 & c_{23} \end{pmatrix} \begin{pmatrix} c_{12} & s_{12} & 0 \\ -s_{12} & c_{12} & 0 \\ 0 & 0 & 1 \end{pmatrix} \\ &= \begin{pmatrix} c_{12}c_{13} & s_{12}c_{13} & s_{13}e^{-i\delta_{CP}} \\ -s_{12}c_{23} - c_{12}s_{23}s_{13}e^{i\delta_{CP}} & c_{12}c_{23} - s_{12}s_{23}s_{13}e^{i\delta_{CP}} & s_{23}c_{13} \\ s_{12}s_{23} - c_{12}c_{23}s_{13}e^{i\delta_{CP}} & -c_{12}s_{23} - s_{12}c_{23}s_{13}e^{i\delta_{CP}} & c_{23}c_{13} \end{pmatrix} \end{aligned}$$

The probability of a neutrino to change its flavor after a free propagation in vaccum is given by the following expression

$$P_{\nu_l \leftarrow \nu_{l'}} \approx \sum_{ij} U^{l',i}{}_{PMNS}(U^{l,i}{}_{PMNS})^*(U^{l',j}{}_{PMNS})^* U^{l,j}{}_{PMNS}\; e^{-i\frac{\Delta m_{ij}{}^2}{2}\frac{L}{E}} \tag{1.2}$$

In the three flavor neutrino framework, there are six independent oscillation parameters, the three mixing angles, the CP violation phase from the PMNS matrix and the two neutrino mass squared differences.

$$\Delta m_{21}{}^2 = m_2{}^2 - m_1{}^2 \tag{1.3}$$
$$\Delta m_{31}{}^2 = m_3{}^2 - m_1{}^2 \tag{1.4}$$

The third mass square difference is a linear combination of the other two $\Delta m_{32}{}^2 = \Delta m_{31}{}^2 - \Delta m_{21}{}^2$. Furthermore, solar neutrino experiments have shown that m_2 is larger than m_1. Therefore, this definition means that there are two possibilities for the ordering of the neutrino masss, normal(m_3 is the heaviest) and inverted (m_3 is the lightest).

The CP violation phase δ_{CP} gives rise to asymmetries between neutrino oscillations and anti-neutrino oscillations if $\sin\delta_{CP} \neq 0$. The magnitude of CP asymmetry is determined by the invariant

$$J_{CP} = \frac{1}{8}\cos\theta_{13}\sin 2\theta_{12}\sin 2\theta_{23}\sin 2\theta_{13}\sin\delta_{CP} \approx 0.033\sin\delta_{CP}[1][2] \qquad (1.5)$$

and could be large compared to the quark sector value ($J_{CP} \approx 3 \times 10^{-5}$). If the CP violation occurs in neutrinos, it should be one of the contributions to explain why today's universe is primarily comprised of matter instead of being comprised of equal parts matter and antimatter.

1.2 Neutrino beam

1.2.1 J-PARC neutrino beam facility

J-PARC(Japan Proton Accelerator Reserch Complex) is an accelerator research facility. It has three proton accelerators which are LINAC(400MeV), RCS(Rapid Cycling Synchrotron, 3GeV) and MR(Main Ring Synchrotron, 30GeV). An intense muon neutrino beam is produced by using MR. The proton beams are directed westward through the primary beam line and strike a graphite target to produce charged pions. The charged pions are focused under the effect of three magnetic horns. The pions decay in a 96 m decay volume and produce a neutrino beam. By switching the polarity of the horn current, either of the neutrino or anti-neutrino beam is selected. With the forward horn current mode(FHC), the neutrino beam is produced. With the reversed horn current mode(RHC), the anti neutrino beam is produced. The muon neutrinos can penetrate a beam dump composed of larde graphie blocks and are detected by near detectors and the Super-Kamiokande, while the other particles such as the remaining protons and undecayed pions are absorbed by the dump. The profile of the muons that remain in the beam is measured by a muon detector, which is called Muon-Monitor(MUMON) and is used as an indirect monitor of the neutrino beam properties. The overview of the J-PARC neutrino beam facility is shown in Figure 1.2.

1.2.2 Off-axis method

The off-axis method is applied in the T2K experiment. The neutrino beam is aimed 2.5° away from the target to the far detector axis in order to optimize the neutrino energy spectrum. This configuration produces a narrow band beam by the kinematics of pion decays. The angle of 2.5° is set so that the spectrum has a peak at the first oscillation maximum around 600 MeV, as shown in Figure 1.3(left).

1.2.3 Bunch structure

The timing structure of the J-PARC neutrino beam is shown in Figure 1.3(right). It has 2.48-second-period spill structure and each spill contains 8 bunches with

581ns gaps.

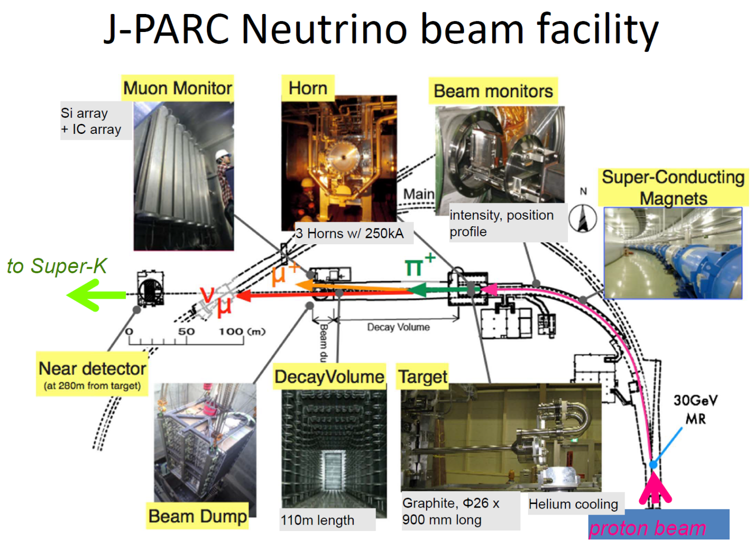

Figure 1.2: The J-PARC neutrino beam facility

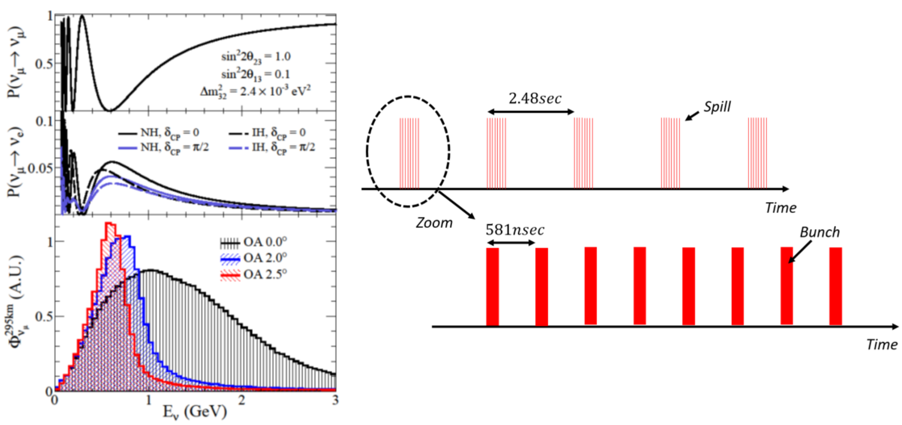

Figure 1.3: The probability of the neutrino oscillations, the muon neutrino flux(left) and the timing structure of the J-PARC neutrino beam(right).

1.3 Detectors

1.3.1 INGRID

INGRID(Interactive Neutrino GRID) is an on-axis near detector and measures the neutrino beam direction and intensity by detecting neutrino interaction events[4]. It is located 280 meters downstream from the graphie target, where the spatial width(1σ) of the neutrino beam is about 5 meters. For this reason, it is designed to sample the beam in a transverse section of 10 m $\times$ 10 m with 14 identical modules arranged as two groups along the horizontal and vertical axis. Each of the modules consists of a sandwich structure of nine iron target plates and 11 tracking scintillator. They are surrounded by veto scintillator planes to reject charged particles coming from outside the modules.

1.3.2 ND280

ND280 is a magnetized off-axis near detector and measures the neutrino beam's prosperities prior to the neutrino oscillation. It can be used to predict the neutrino event rate and energy spectrum at Super-Kamiokande. As well, interaction rates or cross sections for several neutrino interaction channels in the 100 MeV to a few GeV energy range are measured to constrain their uncertainties. ND280 contains several detectors inside the magnet as shown in Figure 1.5. They are Pi-Zero Detector(P0D)[5], Time Projection Chamber(TPC)[6], Fine Grained Detector(FGD)[7], Electromagnetic Calorimeter(ECal)[8], Side Muon Range Detector(SMRD)[9]. ND280 is, same as INGRID, located 280 meters downstream from the graphie target in J-PARC. The direction toward which ND280 is installed is the off-axis angle of 2.5 degrees same as Super-Kamiokande. The ND280 is mainly sensitive to the forward scattered muons because the TPCs are located only upstream and downstream of the FGDs.

1.3.3 Super-Kamiokande

Super-Kamiokande is a water Cherenkov detector which is located in Hida-shi, Gifu Prefecture, Japan.[10] Its location is 295 km away from the beam production target. This is used for not only T2K but also proton decays and studies of neutrino from various sources. The Super-Kamiokande detector consists of a stainless-steel tank, 39.3m diameter and 41.4m tall, filled with 50,000 tons of ultra pure water. More than 11,000 photo-multipliers are installed on the tank wall and detect the cone of Cerenkov light as a ring. Muon events and electron events are distinguished based on their ring shapes. For example, an electron makes an electromagnetic shower and muon does not. Thus an electron makes a fuzzy shape and a muon makes a clear shape.

1.3.4 WAGASCI

WAGASCI is a neutrino detector which enables the measurement of cross section on H_2O [11]. It has been developed for the T2K-WAGASCI project. The purpose of the project is to improve the understanding of the neutrino-nucleus interaction at around 1 GeV and reduce uncertainties of the oscillation analysis. ND280 consists of H_2O and CH targets while Super-Kamiokande consists of H_2O targets. The difference of the target materials induces uncertainties of neutrino-nucleus interactions which give a source of systematic errors. Furthermore, ND280 can measure mainly forward scattering events while the Super-Kamiokande has 4 π angular acceptance. The difference of the acceptance also contributes to the systematic errors. Therefore it is essential to understand the differences in neutrino cross-sections between H_2O and CH targets with a large phase space. Because this project is the main part of this thesis, its detail is explained in Chapter 2.

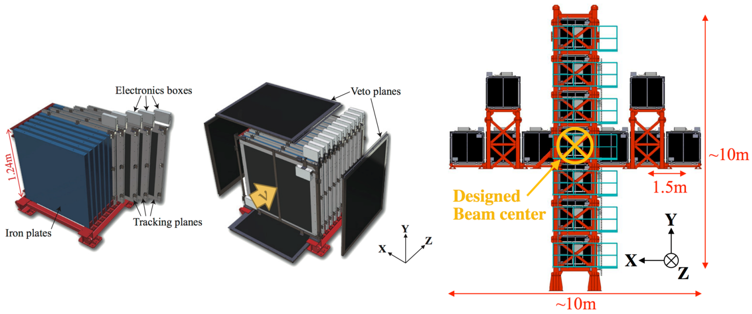

Figure 1.4: Schematic view of one of the INGRID modules(left) and the module arrangement(right).The center of the cross corresponds to the designed neutrino beam center.

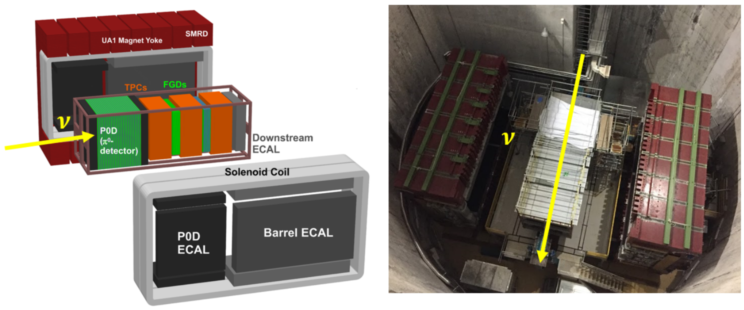

Figure 1.5: Schematic view of the ND280(left) and the picture of the detector(right). The magnets in the picture are opened. They are closed when the ND280 is operated.

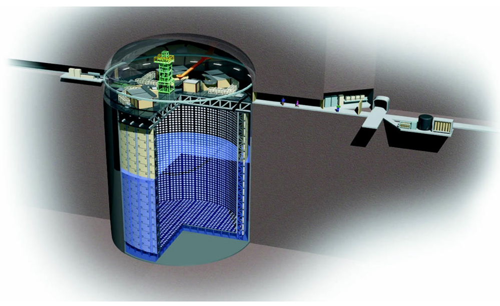

Figure 1.6: The view of Super-Kamiokande

Chapter 2

T2K-WAGASCI project

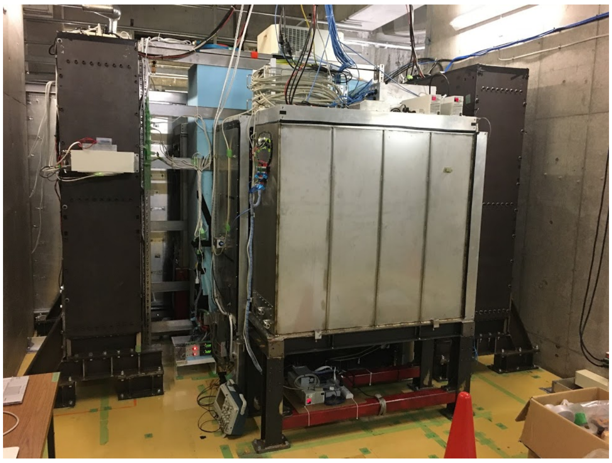

Figure 2.1: Picture of the detector configuration of the T2K-WAGASCI project.

The T2K-WAGASCI project started to reduce uncertainties in the T2K experiment by improving the understanding of the neutrino interaction. For this purpose, we measure the charged-current neutrino cross section ratio between H_2O and CH with a large phase space. It was an independent project named the WAGASCI project, but it was integrated in the T2K experiment in 2019. Figure 2.1 is a picture of the detector configuration of the T2K-WAGASCI project. The detail of the project is explained in this chapter.

2.1 Physics motivation

The understanding of neutrino interactions plays an important role in reducing systematic errors on the neutrino oscillation measurement. In this section, the basis of neutrino interactions is described.

2.1.1 Neutrino interaction

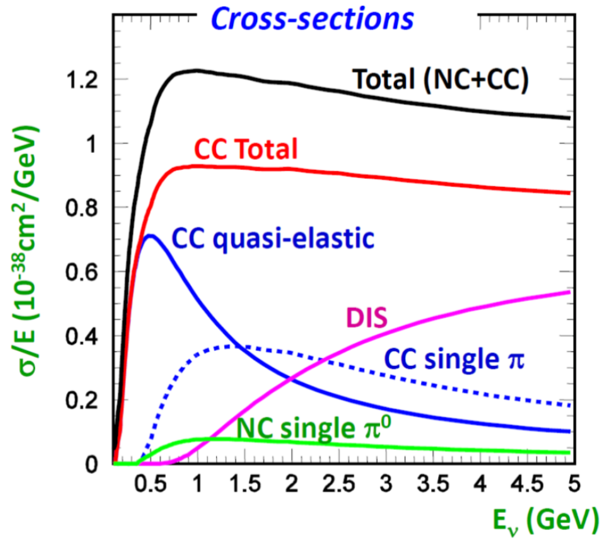

Figure 2.2: The cross sections of neutrino-nucleus interactions for the energy range up to 5 GeV. They were computed by the Monte Carlo simulation.[3]

Neutrinos are electrically neutral and have no color charge. Hence, they interact only via weak interaction. Weak interaction results from the exchange of intermediate vector bosons, $W^{\pm}$ and Z. Charged current(CC) interactions are mediated by the $W^{\pm}$ boson and neutral current(NC) interactions are mediated by the Z boson. We focuss on CC interactions.

Figure 2.2 shows the cross sections of neutrino-nucleus interactions for the energy range up to 5 GeV. They were computed by the Monte Carlo simulation. CCQE (charged current quasci elastic) interaction has the largest cross-section at the energy of the order of 1 GeV, therefore it is the dominant interaction in the T2K experiment. CCQE has a simple topology and is expressed as below(Figure 2.3, left);

$$\nu_l + n \to l^- + p \qquad (l = e, \mu, \tau) \tag{2.1}$$

Because the incident neutrino direction is well known in the accelerator-besed neutrino experiment such as T2K, we can reconstruct the neutrino energy using outgoing lepton kinematics. Assuming the target nucleon is at rest, the neutrino energy can be reconstructed as

$$E_\nu = \frac{m_n E_l + \frac{1}{2}({m_p}^2 - {m_l}^2 - {m_n}^2)}{m_n - E_l + p_l \cos\theta_l} \tag{2.2}$$

where E_ν is energy of neutrino, m_n is a mass of a neutron, m_p is a mass of a proton, E_l, p_l, θ_l are energy, momentum and angle to the beam direction of the lepton.

CC1π (charged current single pion) is the second dominant interaction in the T2K experiment. A neutrino excites a nucleon to a baryonic resonace state, mainly Δ baryon, which decays into a final state with a single pion and a nucleon. This process is expressed as below;

$$\nu_l + N \to l^- + N' + \pi \qquad (l = e, \mu, \tau) \tag{2.3}$$

where N, N' is proton or neutron. Figure 2.3(right) shows one of the possible processes which is expressed as below;

$$\nu_l + p \to \Delta^{++} + l^- \to l^- + p + \pi^+ \qquad (l = e, \mu, \tau) \tag{2.4}$$

This process is three-body scattering and the energy of the outgoing lepton should be smaller than expected in the CCQE interaction. Therefore it can be a background when the pion is not detected and we misrecognize it as CCQE. However this is one of the signal events of T2K because the neutrino energy is reconstructed by assuming a two body scattering with Δ recoil.

CCDIS (charged current deep inelastic scattering) occurs at higher neutrino energy region, where neutrinos directly interact with quarks inside a nucleon. Free quarks cannot be seen due to color confinement and this interaction results in hadronisation as shown in Figure 2.4.

Neutrino-nucleus interactions depend on not only the neutino energy but also the nucleus target. These interaction modes are constructed by assuming a free nucleon. When we use the heavy nucleus target such as carbon(C) and oxygen(O), the neutrino interactions are influenced by the nuclear effects. However the effect is not understood accurately and it become a source of the systematic errors for the T2K experiment. More precise measurements are needed to improve the model which explains all the experimental data.

In the T2K experiment, ND280 consists of H_2O and CH targets while Super-Kamiokande consists of H_2O targets. Thus it is crucial to understand the difference in neutrino cross-sections between H_2O and CH targets. Futhermore ND280 is mainly sensitive to the forward scattered muons while the Super Kamiokande has 4π acceptance. It is also important to understand the difference. For these reasons, we study the difference in neutrino cross sections between H_2O and CH targets and measure them with a large phase space.

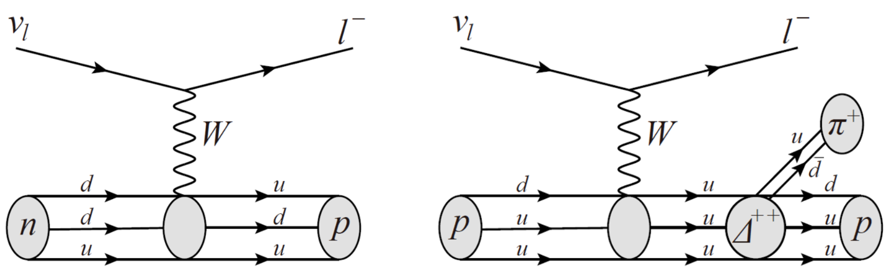

Figure 2.3: Diagrams of CCQE(left) and CC1π(right)

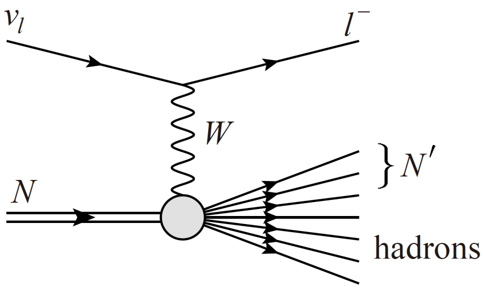

Figure 2.4: Diagrams of CCDIS

2.2 Experimental apparatus

2.2.1 Detector design

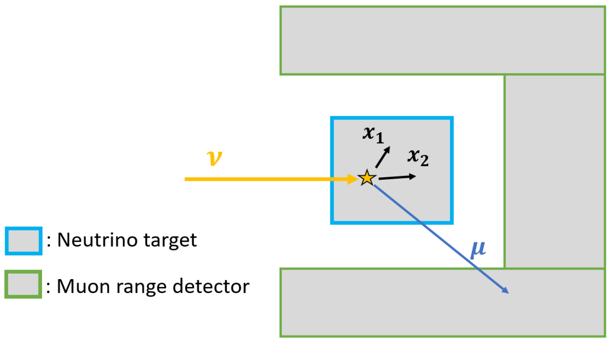

Figure 2.5: Design for the cross section measurement

Figure 2.5 shows a design for the cross section measurement. Neutrino detector which consists of plastic scintillator bars is set on the center. It contains the neutrino target materials such as H_2O and CH. When a neutrino interacts with the target, charged particles are generated. The neutrino interaction is identified by detecting tracks of the charged particles through the plastic scintillator bars. Muons are identified and their momenta are measured by muon range detectors (MRDs) around the neutrino detector.

2.2.2 Detector configuration

Figure 2.6 shows the detector configuration and its dimension is described in Figure 2.7. We use two kinds of target detectors. They are named WAGASCI and Proton Module. The WAGASCI module works as a H_2O target and the Proton Module works as a CH target. We also use two kinds of MRDs. They are named WallMRD and BabyMIND.

This detector configuration was optimized based on the Monte Carlo simulation[13]. The target detectors are arranged in parallel to the beam direction. The two WallMRDs are placed at either side of the neutrino targets. As illustrated in Figure 2.6, the WallMRDs increase the acceptance for large angle tracks for the

WAGASCI detectors. Because the Proton Module is installed between the two WAGASCI detectors, it covers similar phase space. Therefore, we exepect to get both events from the CH target and the H_2O one equally. The north WallMRD is shifted to east compared with the south one because the NINJA detector was installed after the other detectors had been installed and we needed a space for the NINJA detector installation. The NINJA(Neutrino Interaction reserch with Nuclear emulsion and J-PARC Accelerator) collaboration studies low energy neutrino-nucleus interactions with nuclear emulsion detector. The NINJA detector(NJ) is installed between the Proton Module and the downstream WAGASCI.

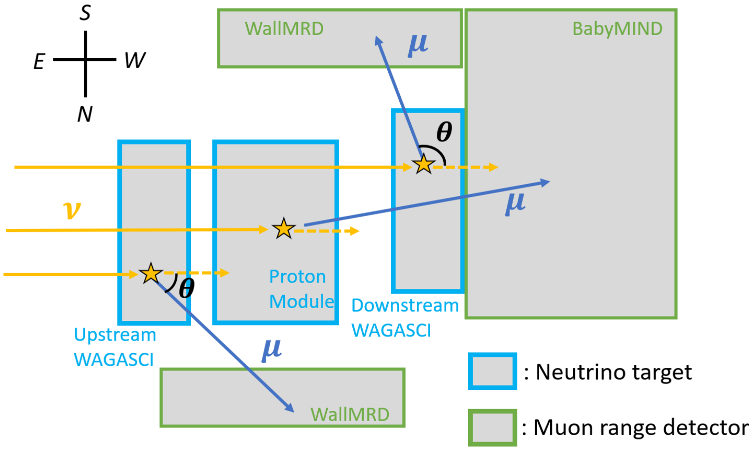

Figure 2.6: Detector configuration.

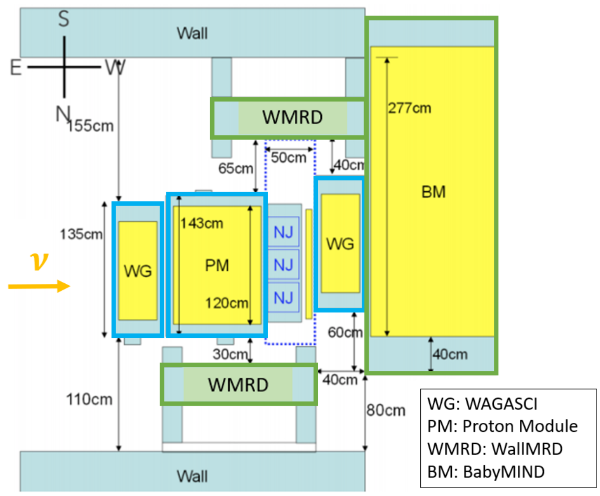

Figure 2.7: Dimension of the detector configuration.

2.2.3 Detector location

These detectors are located on the B2 floor of the J-PARC neutrino monitor hall. The off-axis angle of the WAGASCI location is 1.5 degrees and slightly different to the 2.5 degrees of ND280. The schematics of the hall and the B2 floor are shown in Figure 2.8. The neutrino fluxes at the WAGASCI location and at the ND280 location are shown in Figure 2.9.

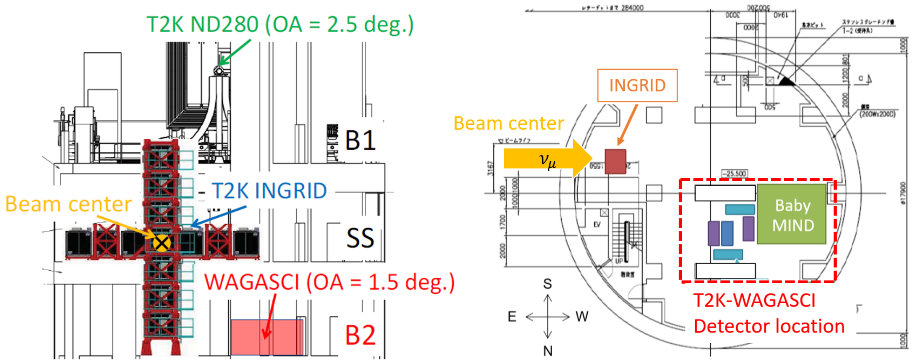

Figure 2.8: The J-PARC neutrino monitor hall(left) and the detector location on the B2 floor(right)

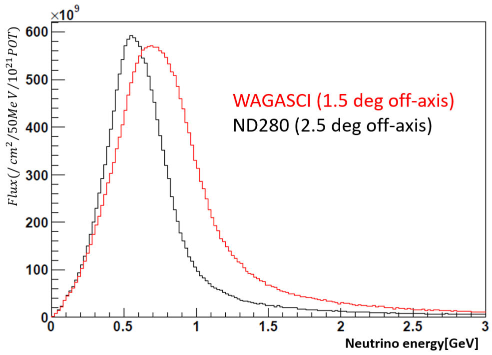

Figure 2.9: Neutrino energy spectrum at the T2K-WAGASCI detector location(red, off-axis 1.5 degree). The spectrum at the ND280 site (black, off-axis 2.5 degree) is also shown.

2.2.4 Proton Module

Proton Module is a fully-active tracking detector which consists of only scintillator strips. It consists of 36 tracking planes surrounded by veto planes (Figure. 2.10, left), where each tracking plane is an array of two types of scintillator strips, one was produced for the K2K SciBar detector[12] and the other is produced for INGRID. The tracking planes are placed perpendicular to the beam axis at 23mm intervals. Each tracking plane is sensitive to either the horizontal or vertical positions because the strips are aligned in one direction. The tracking planes are therefore placed alternating in the horizontal and vertical directions so that three-dimensional tracks can be reconstructed. Scintillation light is read out by a WLS fiber and MPPC. The Proton Module is operated using the T2K near detector electronics/DAQ system.

2.2.5 BabyMIND

BabyMIND is a downstream muon range detector. It has magnetic field to provide the charge identification of secondary particles from neutrino interactions and measure momentum for high energy muon. The detector consists of 33 magnetised metal plates and 18 scintillator modules that measure the position of hits along the spectrometer and the curvature of the track in the magnetic field. Figure 2.11(left) shows a side view of the BabyMIND detector with the alternating magnetised iron plates and scintillator planes. Each scintillator module consists of four planes of polysterene-based extruded scintillator bars, two of the planes are oriented along the horizontal direction, and two of the planes are oriented along the vertical direction as shown in Figure 2.11(left). The horizontal plane size is 2880 × 31 × 7.5 mm^3, with one groove along the length of the plane. The vertical plane size is 1950 × 210 × 7.5 mm^3, with one U-shaped groove along the plane. On each plane, two custom connectors house MPPCs at either side of the horizontal counter and at the top for the vertical counter.

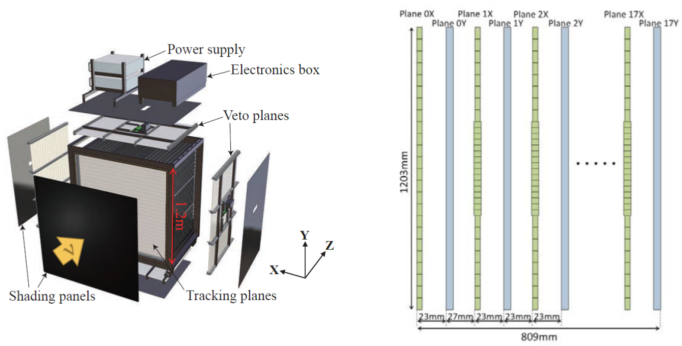

Figure 2.10: Schematic view of the Proton Module(left) and its tracking planes(right)

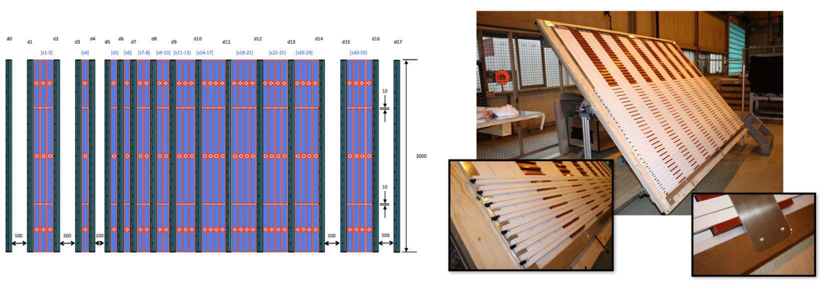

Figure 2.11: Side view of BabyMIND with scintillator planes(grey) and magnetised iron(blue/red) (left) and scintillator module of BabyMIND (right)

2.3 WAGASCI and WallMRD

The WAGASCI module and the WallMRD module are explained in this section. They are main topics of this thesis.

2.3.1 WAGASCI

The WAGASCI module is composed of 1280 plastic scintillator bars which make a three-dimensional grid structure with gaps filled by water (Figure. 2.12, right). The water serves as the neutrino interaction target. A stainless steel tank surrounds the scintillator bars. The size of tank is $460mm \times 1250mm \times 1250mm$ and weighs 0.5 tonne.

The WAGASCI module consists of 16 scintillator tracking planes. Each plane is an array of 80 scintillator bars fixed with ABS frames. The 40 scintillator bars are placed perpendicularly to the beam and the other 40 scintillator bars are placed in parallel to the beam. The combination makes the three-dimensional grid structure and it realizes 4 π angular acceptance for charged paticles. Each scintillator bar is sized as $1020mm \times 25mm \times 3mm$ and half of all the scintillator bars have 50-mm-interval slits to form the three-dimensional grid structure. These thin plastic scintillator bars, the thickness of which is 3mm, are used to reduce the mass ratio of scintillator bar to water because a neutrino interaction in the scintillator bar is a background for the cross section measurement on water. The mass ratio of the scintillator bars to water is 1:4. The total water mass serving as neutrino targets in the fiducial volume of the module is 188 kg. The view of the scintillator bars is shown in Figure 2.13.

The light from scintillator bars is read out by 32-channel arrayed MPPCs via wave length shifting(WLS) fibers. A fiber is glued by optical cement in a groove on surface of a scintillator bar. 32 fibers are gathered together by a fiber bundle at edge of the module and lead scintillation light to a 32 channel arrayed MPPC. The 32-channel arrayed MPPC, S13660 by Hamamatsu Photonics, is used for the WAGASCI module (Figure 2.16, left). Each channel of S13360 has 716 pixels of APD aligned in a shape of circle. Total number of MPPC channels is 1280 for a WAGASCI module.

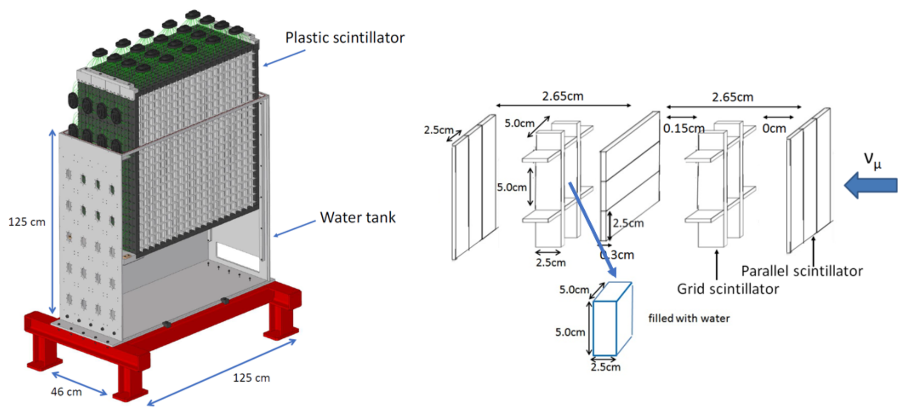

Figure 2.12: Schematic view of the WAGASCI module(left) and its three-dimensional grid structure of plastic scintillator bars(right)

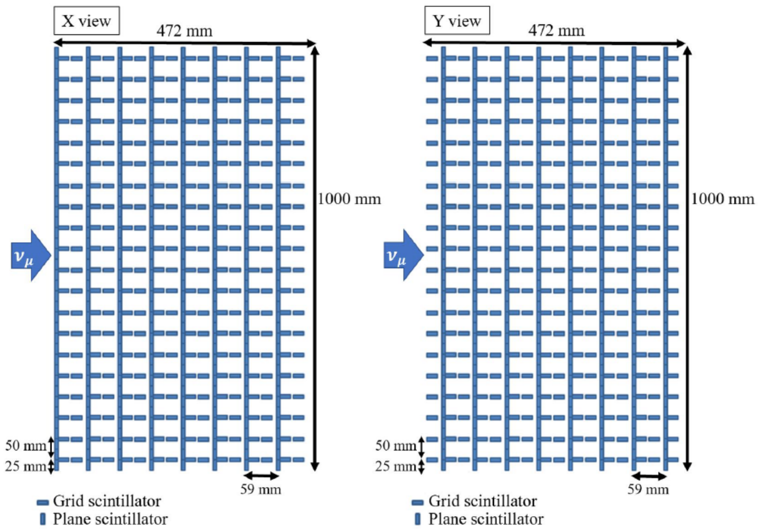

Figure 2.13: View of the scintillator bars of the WAGASCI module from x-direction (left) and y-direction (right).

2.3.2 WallMRD

WallMRD is a side muon range detector to track secondary particles from neutrino interactions. Two WallMRDs are placed at either side of the neutrino targets. It is composed of 11 steel plates and 80 scintillator bars. The scintillator bars are arranged as 10 layers installed in the 13 mm gaps between the 30 mm thick plates. The scintillator layers and the steel plates make a sandwich structure as shown in Figure2.15. The muon momentum can be reconstructed from its range inside the detector. The schematic view of WallMRD is shown in Figure2.14(left) and its weight is ~ 8.5 tonne.

A WLS fiber is glued with optical cement in the S-shape groove as shown in Figure 2.14(right). A minimum bending radius of 30mm is used to ensure the S-shape fiber remained within specification. The size of the scintillator bar is $200mm \times 1800mm \times 7mm$ and the length of fiber is 5m. Both ends of the fiber are glued into optical connectors which are attached to the scintillator and provide an interface to a single-chanel MPPC. The single channel MPPC, S13081-050CS by Hamamatsu Photonics, is used for the WallMRD detector. The MPPC is connected to a dedicated card named the single MPPC Card via 110cm coaxial cables as shown in Figure 2.16 (right). The single MPPC card enables the connection between a frontend board and MPPCs. Total number of MPPC channels is 160 for a WallMRD detector.

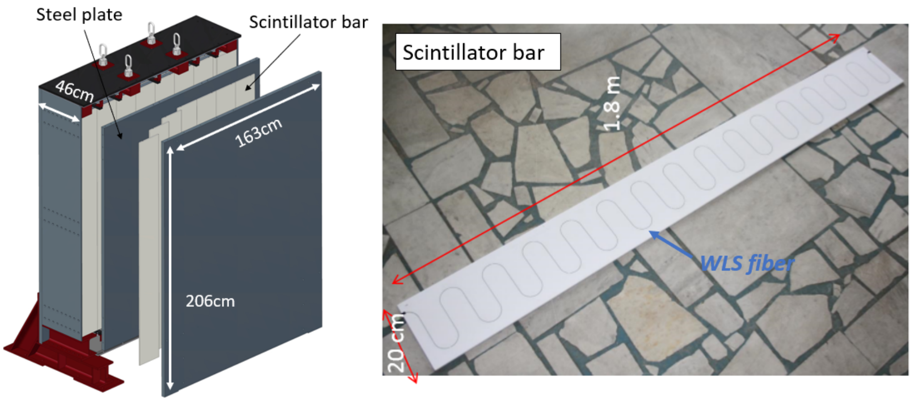

Figure 2.14: Schematic of the WallMRD detector(left) and its scintillator bar(right)

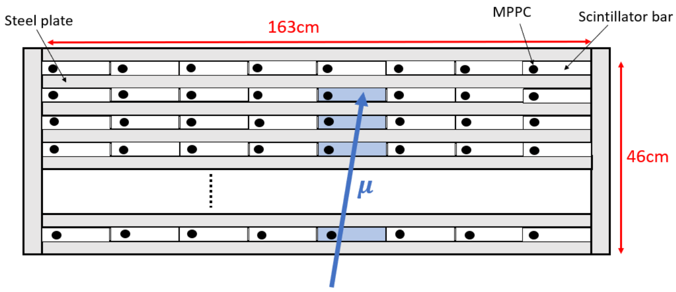

Figure 2.15: The sandwich structure of the WallMRD detector.

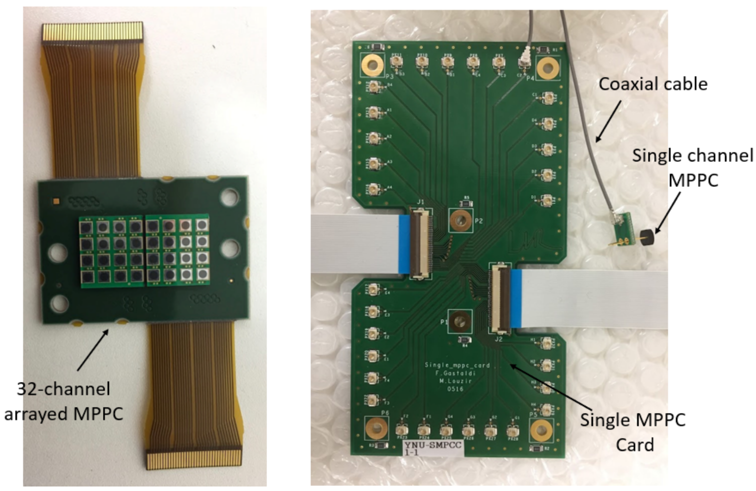

Figure 2.16: 32-channel arrayed MPPC for WAGASCI (left) and single MPPC card for WallMRD (right) to connect single channel MPPCs with a front-end electronics board by coaxial cables

2.3.3 Electronics

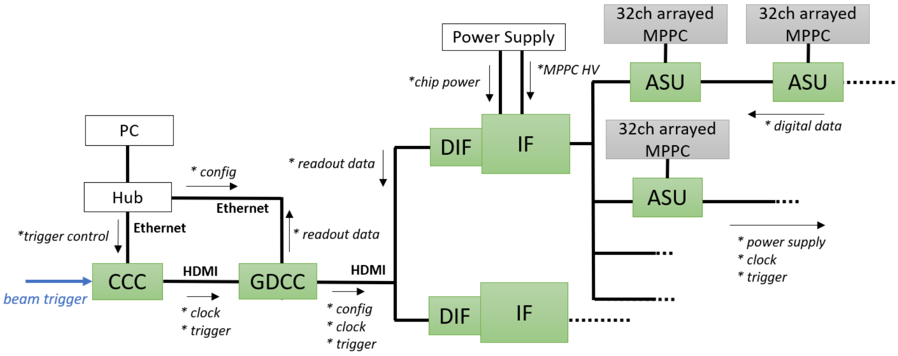

Figure 2.17: Readout scheme of the WAGASCI module

A dedicated readout system for WAGASCI and WallMRD has been developed at Laboratoire Leprince-Ringuet (LLR) of l ' Ecole polytechnique and the University of Tokyo. [14]. It is based on Silicon PM Integrated Read-Out Chip (SPIROC)[16]. SPIROC is a 36-channel self triggered front-end ASIC. A front-end electronics board, Active Sensor Unit (ASU, Figure2.18: left), has been developed with SPIROC. Readout signals from ASU are processed through an interface board (IF, Figure2.19: left) and a detector interface (DIF, Figure2.18: right) which controls SPIROC chips. Giga data concentrator card (GDCC, Figure2.19: right) communicates with DAQ PC and sends the output data from DIF. The whole system is synchronized to a 20ns clock, called the fast clock, by Clock Control Card(CCC). DIF receives and counts fast clocks and makes a 580-period clock which is called the slow clock. The slow clocks are sent to each ASU. The electronics readout scheme is shown in Figure 2.17. These electronics boards are installed to the WAGASCI modules and the WallMRD detectors as shown in Figure 2.20 and 2.21. Two DIFs, two IFs and forty ASUs are used for a WAGASCI module and two DIFs, two IFs and six ASUs are used for a WallMRD detector. The relationships between scintillators and ASUs for each detector are shown in Figure 2.22 and 2.23. An ASU board for WAGASCI reads out 32 channels from a fiber bundle and that for WallMRD reads out 30 or 20 channels from coaxial cables.

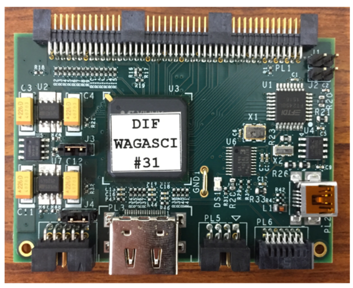

Figure 2.18: Pictures of ASU(left) and DIF(right). SPIROC2D is mounted on the ASU board.

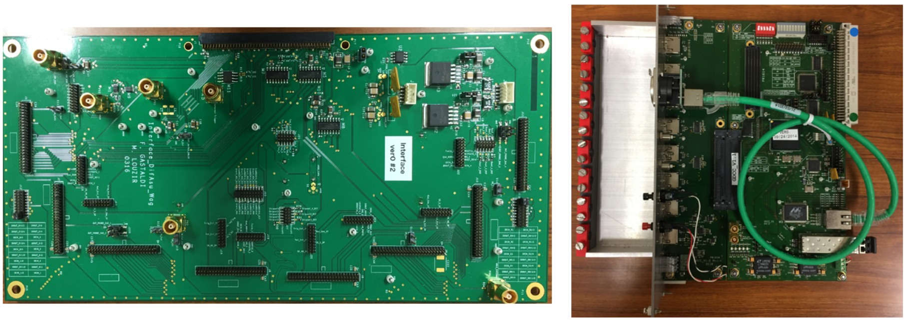

Figure 2.19: Pictures of Interface(left) and GDCC(right).

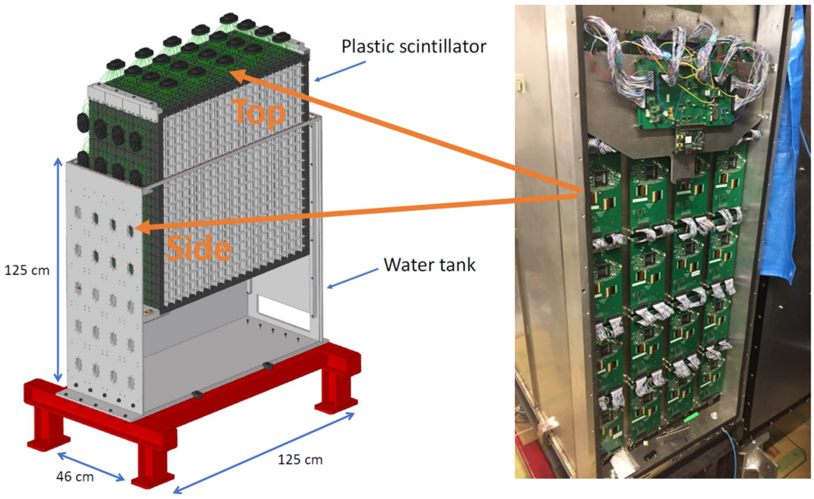

Figure 2.20: Electronics on the WAGASCI module

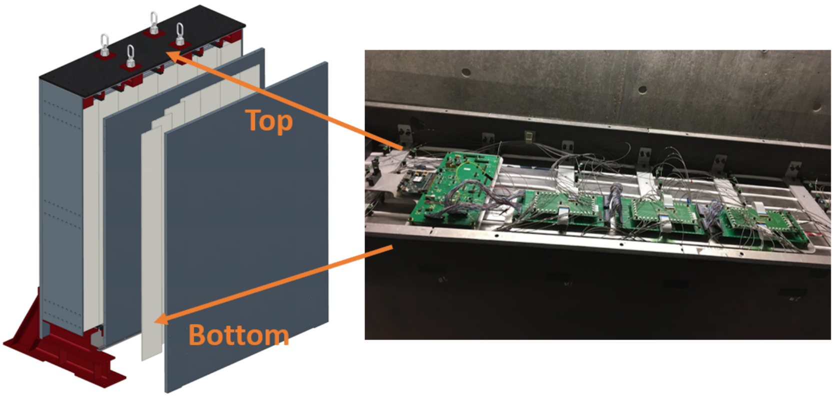

Figure 2.21: Electronics on the WallMRD detector

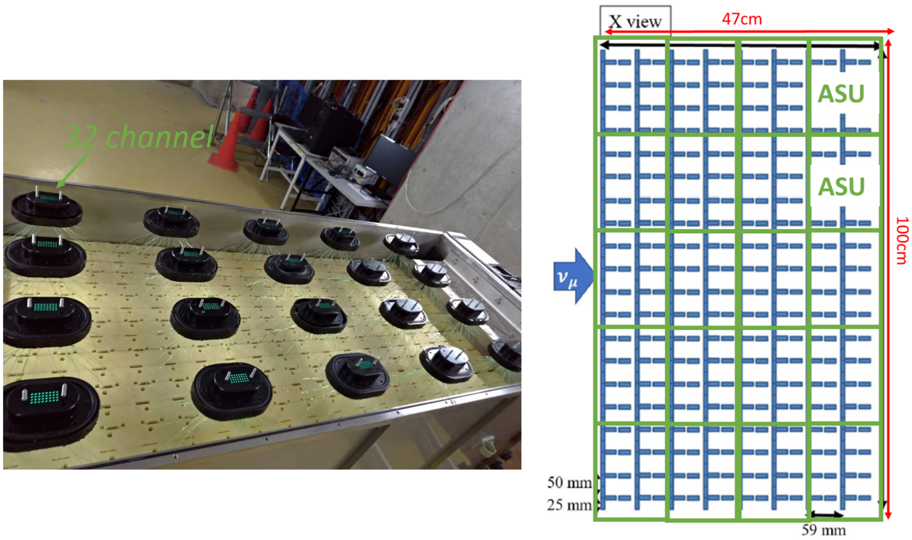

Figure 2.22: Picture of the fiber bundles of WAGASCI(left) and the relationship between scintillators and ASUs for WAGASCI(right)

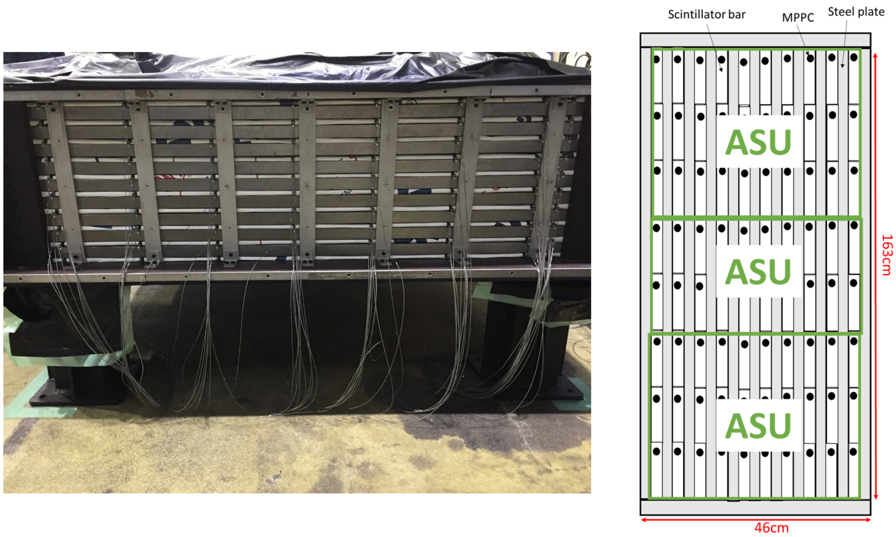

Figure 2.23: Picture of the cross-section of WallMRD(left) and the relationship between scintillators and ASUs for WallMRD(right)

SPIROC2D

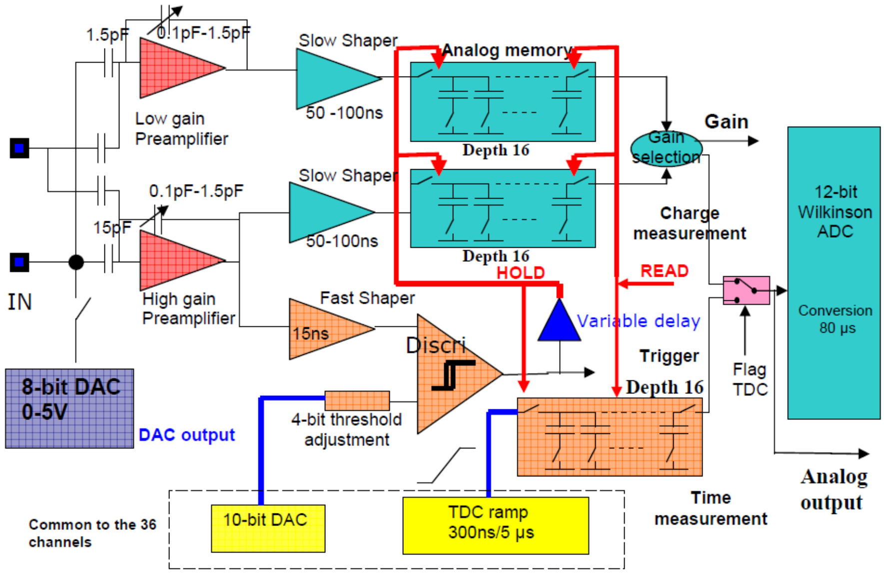

Figure 2.24: Block diagram of analogue part of SPIROC2

A front-end chip called SPIROC has been designed for an ILC prototype hadronic calorimeter with SiPM readout. SPIROC2D is a version of SPIROC. SPIROC2D has been developed with the requirements of large dynamic range, low noise, low consumption, high precision and large number of readout channels. Figure 2.24 shows the block diagram of the analog parts for a channel in SPIROC2D. SPIROC2D is an auto-triggered, bi-gain, 36-channel ASIC which allows to measure on each channel the charge from one to 2000 photoelectrons and the time with a 100ps accurate TDC. The two preamplifiers allow the required dynamic range and are followed by a trigger line made of a fast shaper and a discriminator. An analog memory array with a depth of 16 for each is used to store the time information and the charge measurement. A 12-bit Wilkinson ADC is embedded to digitize the analog memory contents (time and charge on 2 gains). An input DAC is implemented in SPIROC to adjust bias volage of individual MPPC. Performance of MPPC is sensitive to temperature and bias voltage. The gain of MPPC is a sensitive probe to monitor the stability of MPPC performance. Input DAC makes it possible to tune MPPC gains channel by channel.

Analog memory array

The charge and the TDC information is stored in an analogue memory (SCA) with a depth of 16 capacitors as shown Figure 2.24. When a trigger is issued, data can be captured in the current column by means of a "Track and Hold Cell" inside the SCA. When the next edge of slow clock is detected, it closes the capture window and the data column moves to the next at the same time for all 36 channels. The schematic of data storage system is shown in Figure 2.25.

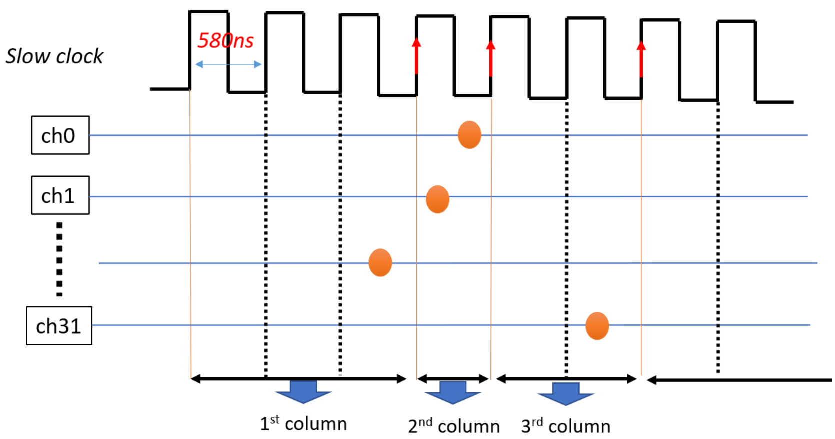

Figure 2.25: Schematic of data storage system

Timing measurement system

When a trigger is issued, coarse time information is stored in digital memory and fine time information is stored in analog memory. The former is called BCID (Bunch Crossing ID). It is the number of the slow clock after the rising edge of the start-acq signal which opens a data acquisition gate. The latter is gotten by the TDC ramp which is a ramp signal. The TDC ramp goes up when BCID is odd and goes down when BCID is even as shown in Figure 2.26.

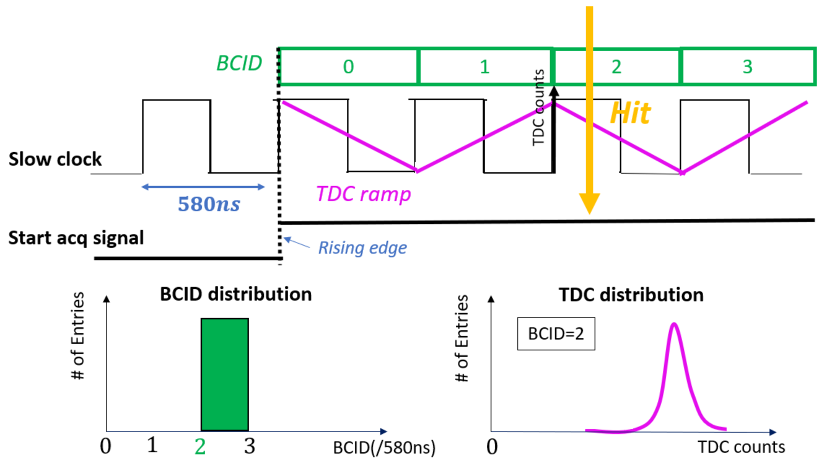

Figure 2.26: Schematic of timing measurement system

Link between SPIROC and DAQ

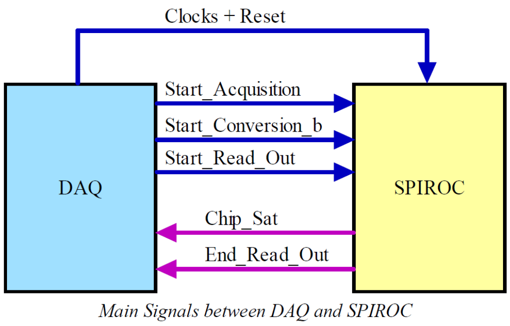

Figure 2.27: Communication between SPIROC and the DAQ

The digital part of SPIROC consists of three parts; Acquisition, Conversion, Readout. They are activated by signals from the DAQ as shown in Figure 2.27. There are two cases to stop the acquisition. One case is that the acquisition ends by the time the DAQ system sets (Figure2.28, left). The other case is that the acquisition ends by a chip-saturation signal (Figure2.28, right). When all the 16 columns are closed, the signal rises up. Therefore the acquisition become a short time when noise rate is high.

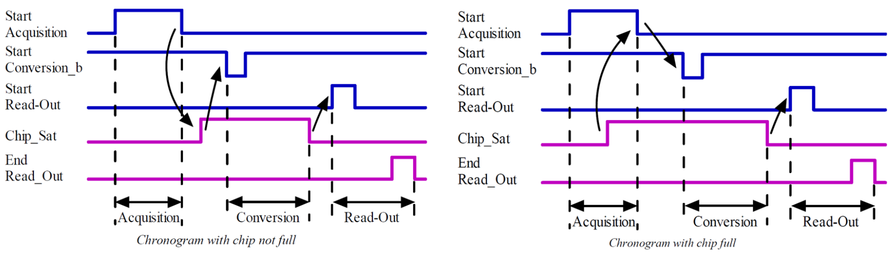

Figure 2.28: Schematic of the DAQ signals in case that the chip does not get full(left) and in case that the chip gets full (right).

Threshold problem

The auto-trigger is taken on the high gain path with a high-gain fast shaper followed by a discriminator. However the polarity of comparator is upside down due to a design error. In the normal case, if the signal is "over" the threshold, the acquisition is triggered. In the case of SPIROC2D, if the signal is "below" the threshold, the acquisition is triggered. Figure 2.29 shows two signals over the respective thresholds. The blue lines show where the threshold should be: in this case only signals above the threshold value trigger acquisition. The red lines show where the threshold actually is: in this case only signals below the threshold value trigger acquisition.

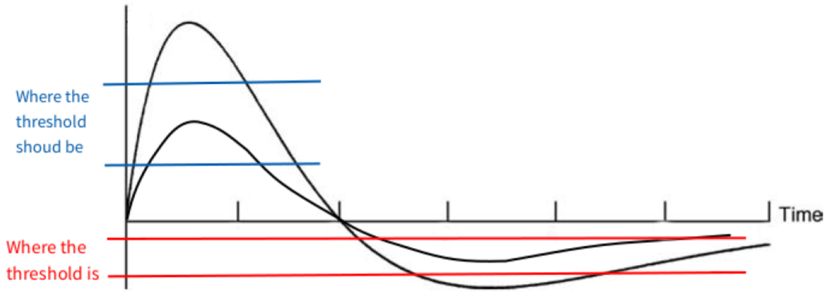

Figure 2.29: Problem due to the wrong position of comparator of SPIROC2D.

Triggering system

The readout system is synchronized to the neutrino beam timing using two timing signals, *pre-beam trigger* and *beam trigger*. The pre-beam trigger signal arrives 100 ms before the arrival of the beam trigger signal and the beam trigger signal arrives about 30 μs before the neutrino beam. With receipt of the beam trigger, CCC sends DIF a digital signal to open an acquisition gate for the neutrino beam data. After the acquisition gate for the neutrino beam is closed, periodic acquisition gate is opened to accumulate data for monitoring the detector stability. Figure 2.30 shows a schematic timing chart for the timing synchronization.

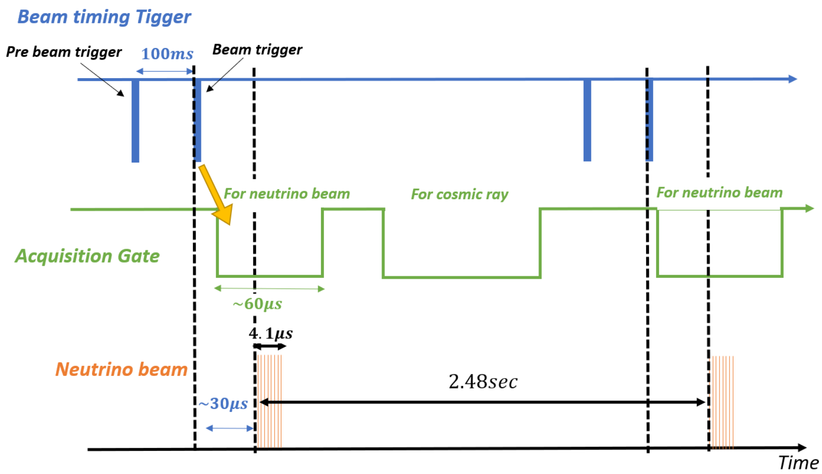

Figure 2.30: Beam trigger chronograph

2.3.4 Expected timing resolution

We estimated the timing resolutions of WAGASCI and WallMRD. The resolution of the hit time recorded in SPIROC2D has contributions from scintillator ($\sigma_{scintillator}$) and readout (σ_{SPIROC}).

$$\sigma_t = \sqrt{{\sigma_{scintillator}}^2 + {\sigma_{SPIROC}}^2}. \tag{2.5}$$

Because WallMRD has two readouts per a scintillator, the timing resolution becomes $1/\sqrt{2}$. The timing resolutions of scintillators for both detectors were measured in 2017[20]. The results are summarized in Table 2.1.

We measured the contribution from readout, σ_{SPIROC}, with a pico pulse laser and a LED. The pico pulse laser was used for a high quality timing measurement with a fixed light input. The light input dependence was measured with a LED.

Detector	$\sigma_{scintillator}$
WAGASCI	1.95 ns
WallMRD	1.15ns

Table 2.1: Time resolution of the scintillators

Measurement with pico pulse laser

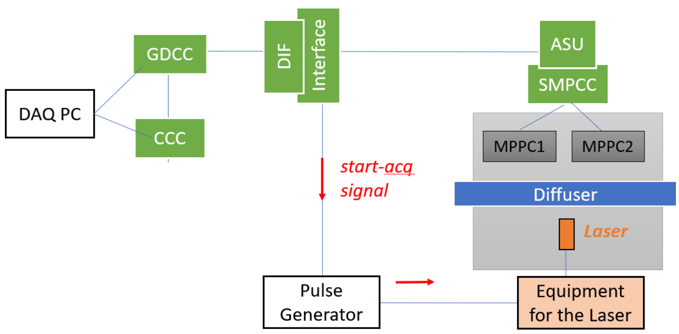

Figure 2.31: Test setup with the pico pulse laser

Figure 2.31 shows a diagram of the test setup with the pico pulse laser. Two MPPCs were used with a single MPPC card and the 20 cm coaxial cables. The signals of both MPPCs were analyzed. A diffuser was inserted between the laser and the MPPCs to inject the light to both MPPCs. The threshold of SPIROC was set to around 4.5 p.e. to avoid the effect of dark noise.

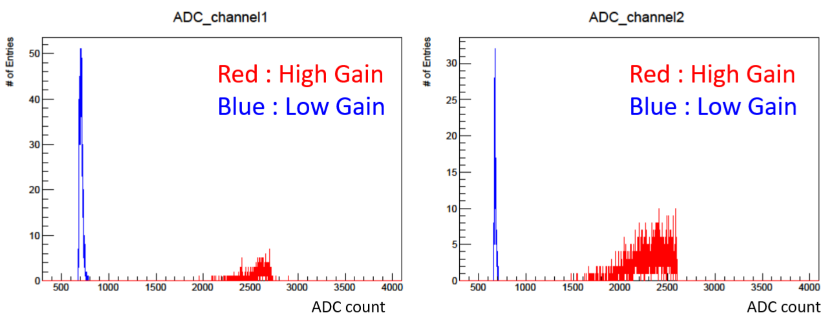

Figure 2.32: ADC distributions of the two MPPC channels.(red: high gain, blue: low gain)

To begin with, the light yields were calculated from the ADC distributions of each MPPC channel. The ADC distributions are shown in Figure 2.32. As explained in section 2.3.3, SPIROC has a bi-gain, high gain(HG) and low gain(LG), and one of the signals of the two preamplifiers is selected and recorded automatically. Therefore two kinds of distributions are shown in the histograms. Light yields were calculated for each distribution and then the two light yields were conbined as follows;

$$LY_{HG,LG} = \frac{(Mean\ of\ ADC\ distribution_{HG.LG}) - (Pedestal)}{(Gain_{HG,LG})} \tag{2.6}$$

$$LY = LY_{HG} \times \frac{N_{HG}}{N_{Total}} + LY_{LG} \times \frac{N_{LG}}{N_{Total}} \tag{2.7}$$

Here, LY is the light yield and N is the number of entries. $N_{Total} = N_{HG} + N_{LG}$ is valid. Before this measurement, dark noise was measured at 0.5 p.e. threshold to calculate the gains. The gain as an unit of the high gain was gotten from the ADC distribution by seeing the difference between the peaks corresponding to 1p.e. and pedestal. The gain was adjusted to about 40 ADC count/p.e. which is the same value as in the actual beam measurement. The gain as an unit of the low gain was calculated from the fact that the gain of the high gain preamplifier is 10 times larger than that of the low gain preamplifier. The measured light yields for each MPPC channel are,

- Channel1 : $Light\ Yield = 51\ p.e.$
- Channel2 : $Light\ Yield = 43\ p.e.$

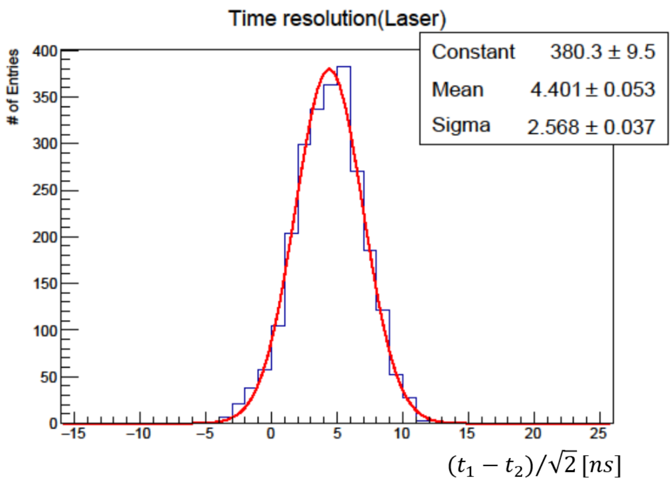

Figure 2.33: Hit timing difference between the two channels

Then, the time resolution was checked. It was calculated by the hit timings of the two MPPC channels. They were subtracted for each light injection and the hit timing differences devided by $\sqrt{2}$ were filled into a histogram. Then the distribution was fitted by a gaussian function as shown in Figure 2.33. The sigma of the fitted gaussian was defined as a time resolution. The measured time resolution is,

- $\sigma = 2.6\ ns$

The results of the measurement are summarized in Table 2.2.

Measured item	Result
Light yield (Channel1)	51 p.e.
Light yield (Channel2)	43 p.e.
Light yield (Mean)	47 p.e.
Time resolution	2.6 ns

Table 2.2: Result of the measurement with the pico pulse laser

Measurement with LED

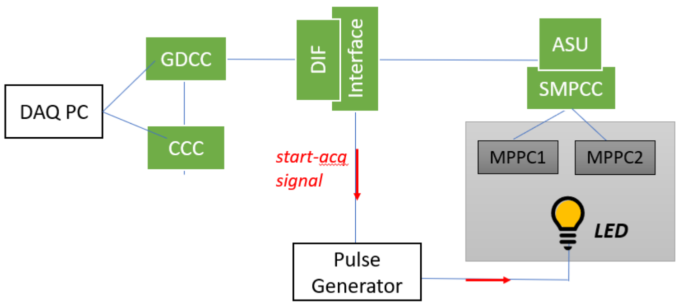

Figure 2.34: Test setup with LED

In order to measure the relationship between time resolution and light yield, a test setup with a LED was constructed as shown in Figure 2.34. The setup and its configuration are almost the same as the case of the pico pluse laser, but the diffuser was not used. The adjustment of light yield was realized by the pulse generator. Figure 2.35 shows the change of time resolution as a funtion of light yield. The light yields used for the horizontal axsis are the mean of the two MPPC channels. The measured resolution is fitted by an inverse function as follows,

$$\sigma = \frac{p0}{LY + p1} + p2 \tag{2.8}$$

where σ is the time resolution and LY is the light yield. p0, p1 and p2 are fitting parameters. The blue point is the result of the pico pulse laser (47 p.e., 2.6 ns), which is consistent with the fitted function.

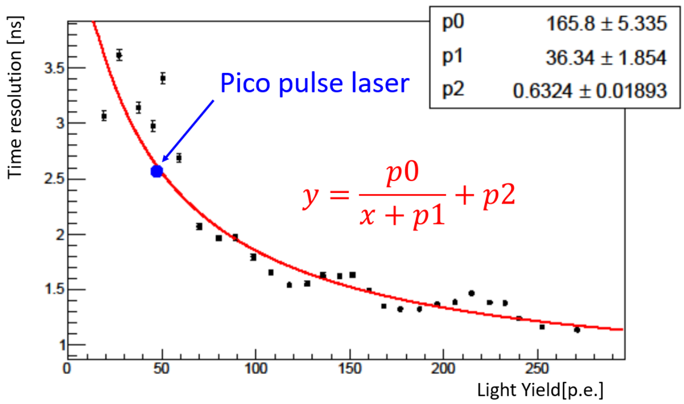

Figure 2.35: Time resolution dependency with light yield

Estimation of the timing resolution

We estimated the timing resolutions of both detectors based on the above measurements. The mean light yield of the WAGASCI scintillator is 13 p.e. and that of the WallMRD scintillator is 20 p.e.[20]. When we substitute these values for the fitting function in Eq.(2.8), the contributions from readout are estimated. The results are summarized in Table 2.3.

Detector	σ_{SPIROC}
WAGASCI	4.0ns
WallMRD	3.6ns

Table 2.3: Timing resolution of SPIROC2D

The timing resolutions of both detectors were estimated using Table 2.1 and Table 2.3 as follows,

$$\sigma_{WAGASCI} = \sigma_t = \sqrt{{\sigma_{scintillator}}^2 + {\sigma_{SPIROC}}^2} = 4.5\ ns \tag{2.9}$$

$$\sigma_{WallMRD} = \frac{\sigma_t}{\sqrt{2}} = \sqrt{\frac{{\sigma_{scintillator}}^2 + {\sigma_{SPIROC}}^2}{2}} = 2.7\ ns \tag{2.10}$$

2.4 History of the WAGASCI experiment

Before the physics run with the detector configuration as shown in Figure 2.6, two pilot run were conducted. In the first pilot run [17] [18], a WAGASCI module was located on axis where the mean energy of neutrino is 1.5 GeV. The WAGASCI module was operated using the INGRID electronics/DAQ system. We collected neutrino beam data from October 2016 to April 2017. The data includes a beam exposure of 7.25×10^{20} protons on target(P.O.T).

In the second pilot run [19], the second WAGASCI module was located 1.5 degrees off-axis. The dedicated electronics and DAQ system were used for the WAGASCI module. We collected anti-neutrino beam data from October 2017 to May 2018. The data includes a beam exposure of 7.25×10^{20} protons on target(P.O.T). A Proton Module and an INGRID module were used as shown in Figure 2.36.

The summary of each run is shown in Table 2.4.

Run	First pilot run	Second pilot run	First physics run
Time	Oct.2016 - Apr.2017	Oct.2017 - May.2018	Nov.2019 - Feb.2020
Beam	Neutrino	Anti-neutrino	Neutrino
Angle at off-axis	On-axis	1.5 degree	1.5 degree
Mean Energy	1.5 GeV	0.86 GeV	0.86 GeV
Beam exposure	7.25×10^{20} P.O.T	8.5×10^{20} P.O.T	5.0×10^{20} P.O.T

Table 2.4: History of the WAGASCI experiment

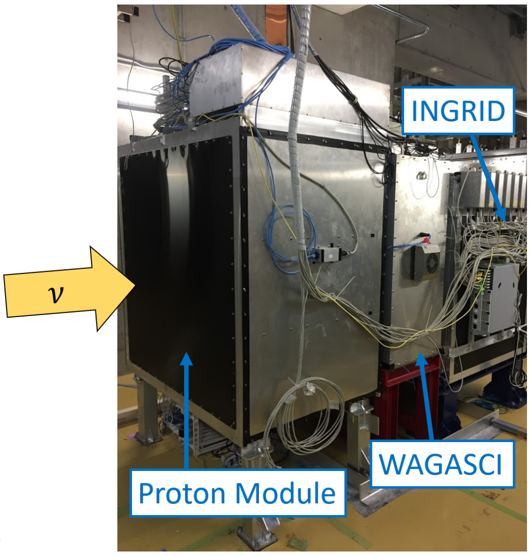

Figure 2.36: Detector configuration of the second pilot run

2.5 Detector installation

The second pilot run finished in May 2018. We started the detector installation for the first physics run in January 2019. The procedure of the detector installation is as follows. (Figure 2.37)

1. Removal of the detectors
2. Installation of the two WallMRDs
3. Water filling of the downstream WAGASCI
4. Installation of the downstream WAGASCI
5. Installation of the Proton Module

6. Water filling and installation of the upstream WAGASCI
7. Installation of the electronics

In order to reflesh the experimental site, we removed all the detectors for the second pilot run. BabyMIND was installed during the second pilot run. First, two WallMRD detectors were installed and then the other modules were installed. Before the installation of the WAGASCI detectors, we filled pure water to them. We filled 600 liters of pure water for a detector. After the detector installation, we did a mass test of the frontrnd board which is discussed in the next chapter.

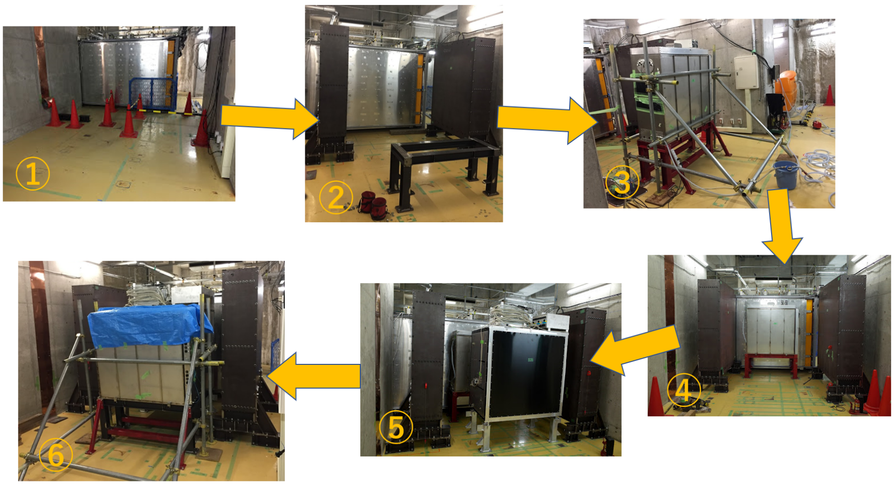

Figure 2.37: Detector installation for the first physics run

2.6 Subject of this thesis

This thesis describes the preparation for the first physics run and its beam measurement. The subject is the dedicated electronics and its timing measurement.

We discuss the preparation for the first physics run in Chapter 3 and 4. We needed to install the dedicated electronics to a WAGASCI detector for the physics run. Before the installation, 40 ASU boards were tested at the University of Tokyo. On the other hand, a problem with a timing measurement was revealed during the second pilot run. The timing measurement system was not synchronized to the beam timing so that we did not have an ability to reconstruct the bunch structure by hit timings. In order to solve the problem, we improved the DIF firmware.

We explain the staus of the physics run in Chapter 5. The timing measurement system of the WAGASCI detector was calibrated using the neutrino beam. The calibration method and its performance is discussed in Chapter 6.

Finally, a performance with the timing information is discussed in Chapter 7. Background events from outside of the WAGASCI detector are rejected using the hit timings of WAGASCI and WallMRD. We developed two methods for the background rejection and they were evaluated by a Monte Carlo simulation.

Chapter 3

Mass test of the frontend board

Figure 3.1: Picture of the ASU mass test at the University of Tokyo. We operated 40 ASUs simultaneously assuming the actual operation

Two WAGASCI detectors were used in the two pilot runs separately and the dedicated DAQ system was not applied to the WAGASCI for the first pilot run. Thus we needed to install the electronics to the WAGASCI. Before the electronics installation, we conducted a mass test of 40 ASUs at the University of Tokyo in April 2019. Each ASU was connected to a 32-channel arrayed MPPC so that the total number of MPPC channel was 1280. We checked the following items;

- Gain tuning
- Threshold curve measurement
- TDC ramp measurement

The gain tuning is important to set an appropriate threshold because the threshold is common to all the channels in a SPIROC. After the gain tuning, we checked threshold curves for each SPIROC. In order to know threshold values corresponding to each photoelectron level, we measured noise rate changing threshold. Furthermore TDC ramp was measured to calibrate its difference. The constructed setups are shown in Figure 3.2 and 3.3.

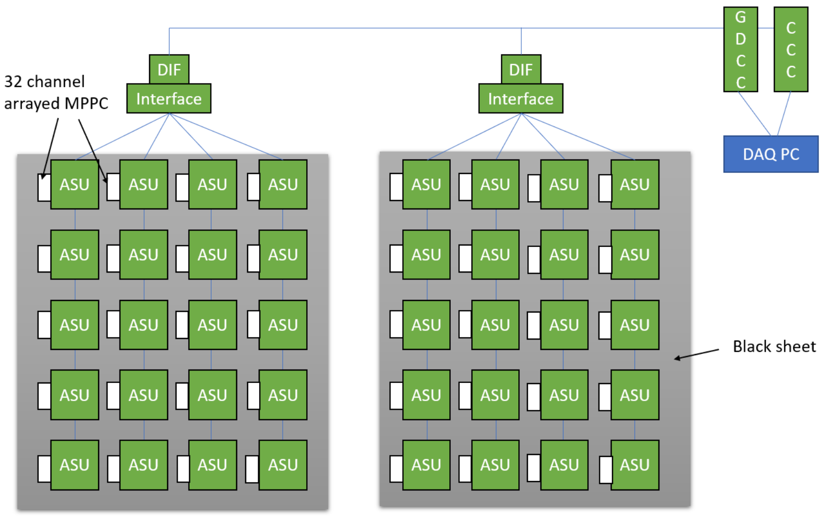

Figure 3.2: Test setup for the gain tuning and the threshold curve measurement.

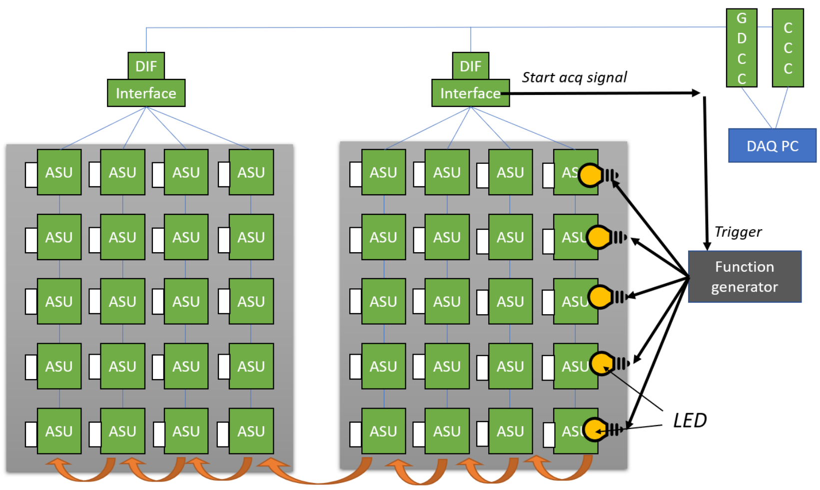

Figure 3.3: Test setup for the TDC ramp measurement. We measured the TDC ramps every five ASUs simultaneously as illustrated.

3.1 Gain tuning

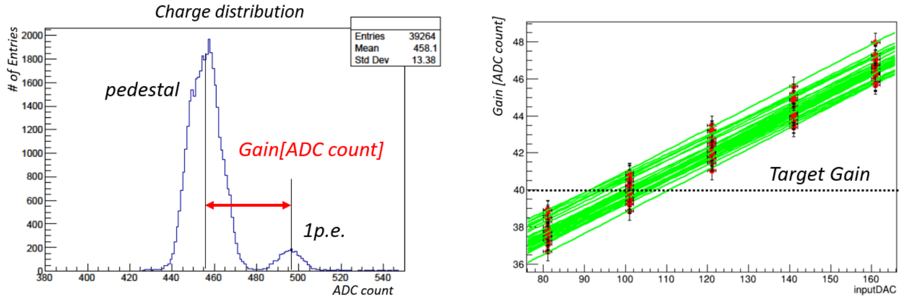

Figure 3.4: An example of the charge distribution of dark noise measurement(left). Gains of 32 channels increase by input DAC(right).

In order to check the ability to adjust all the MPPC gains to a target value using the 40 ASUs, we did a gain tuning test. An input DAC of SPIROC can adjust bias volage of individual MPPC. We measured dark noise with the 0.5 p.e. threshold changing the input DAC. Figure 3.4(left) shows a charge distribution which shows two peaks of 0 p.e.(pedestal) and 1 p.e. equivalent ADC count. The distance of the peaks corresponds to a MPPC gain and it changes by the input DAC as shown in Figure 3.4(right). Using the linearity, we did a gain tuning. The target value was 40 ADC count/p.e. which is applied to the actual beam measurement. The result is shown in Figure 3.5. After the tuning, all the channels were within 10 % of the target value.

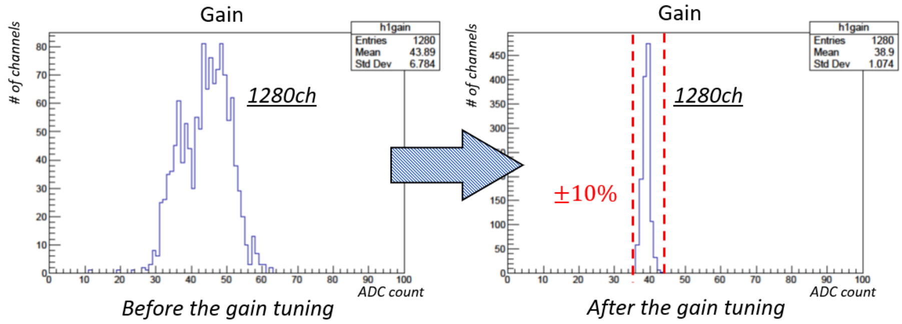

Figure 3.5: Result of the gain tuning. After the tuning, all the channels were within 10 % of the target value.

3.2 Threshold curve measurement

In order to set an appropriate threshold for each ASU, we did a noise rate measurement. Figure 3.6 shows an example of the threshold curve. Because of the threshold problem of SPROC2D explained in section 2.3.3, noise rate decreases when a threshold is lowered. The threshold curve teaches us the threshold values corresponding to each photoelectron level as this example shows. Figure 3.7

shows the threshold curves of the 40 ASUs. We got the information about the threshold values of all the ASUs.

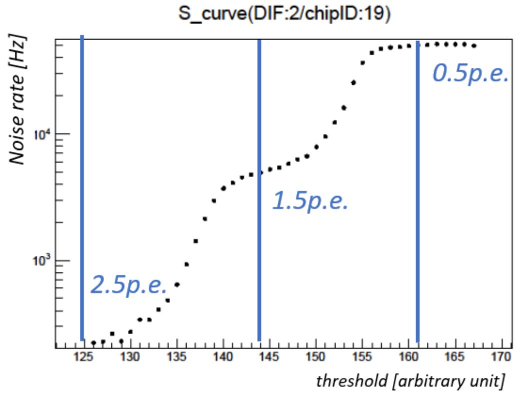

Figure 3.6: An example of the threshold curve. Because of the threshold problem of SPROC2D, noise rate decreases when a threshold is lowered.

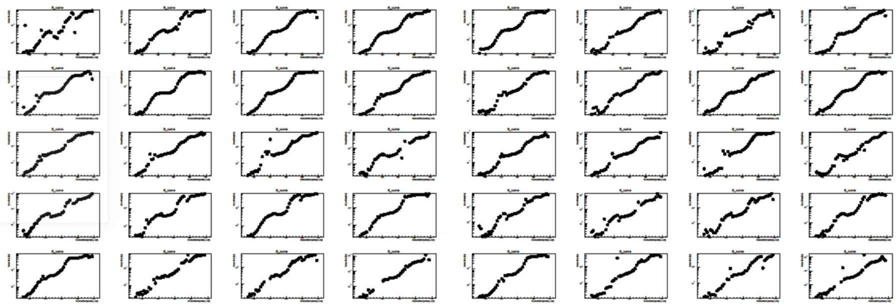

Figure 3.7: Measured threshold curves of the 40 ASUs.

3.3 TDC ramp measurement

We measured TDC ramp slope. Figure 3.8 explains the method of measurement. We injected light which is synchronized to the start-acq signal to each MPPC. The setup is shown in Figure 3.3. We checked a TDC distribution and a peak corresponding to the light injection timing was fitted by a gaussian function. We delayed the injection timing every 40 ns and plotted the mean of the gaussian corresponding to each timing. The slope is obtained by a linear fitting of the plot.

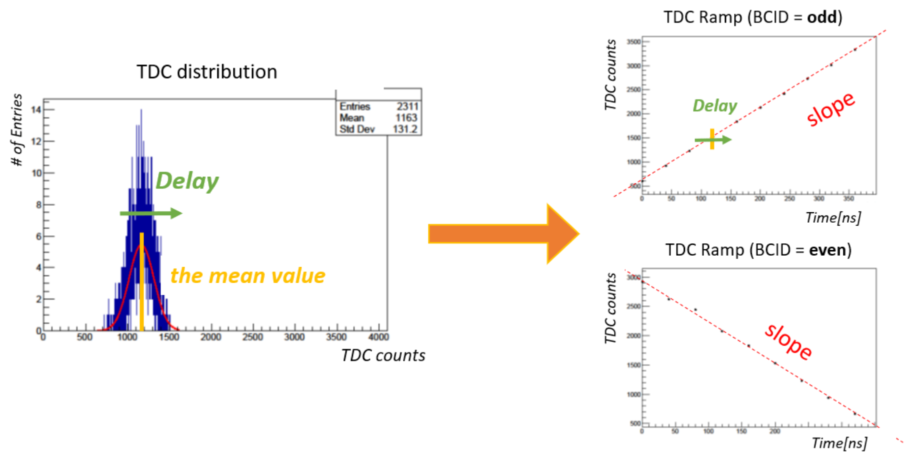

Figure 3.8: Overview of the TDC ramp measurement

According to the block diagram of analogue part of SPIROC2D (Figure 2.24), the TDC ramp depends on SPIROCs but it does not depend on channels and columns. The fact was checked by a measurement of the 40 ASUs. Figure 3.9(left) shows the difference between the slope of each channel and the averaged of 32 channels in the chip. This histogram includes both results of slopes of ramp-up and ramp-down. The channel dependency was confirmed to be small.

We also checked the column dependency by two light injections per an acquisition gate. The hit information of the first injection is stored in the first column and that of the second injection is stored in the second column. The difference between a slope of the first column and that of the second column is shown in Figure 3.9(right). The columm dependency was confirmed to be small.

These results indicate that we do not have to calibrate the TDC ramp for each channel and columm. Therefore we measured the TDC ramp for each ASU. Figure 3.10 shows the distributions of the measured TDC ramp slopes. They include all the ASUs we measured. The maximum of the ramp-up slope is 10.7 TDC count/ns and the minimum of that is 7.2 TDC count/ns. They correspond to 93ps to 139ps per one TDC count. The maximum of the ramp-down slope is |-10.4| TDC count/ns and the minimum of that is |-7.1| TDC count/ns. They correspond to 96ps to 141ps per one TDC count.

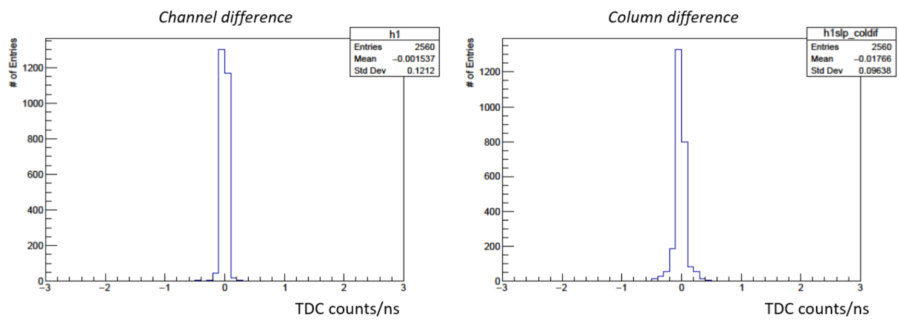

Figure 3.9: Channel dependency(left) and columm dependency(right) of the TDC ramp slope. Both dependencies were confirmed to be small

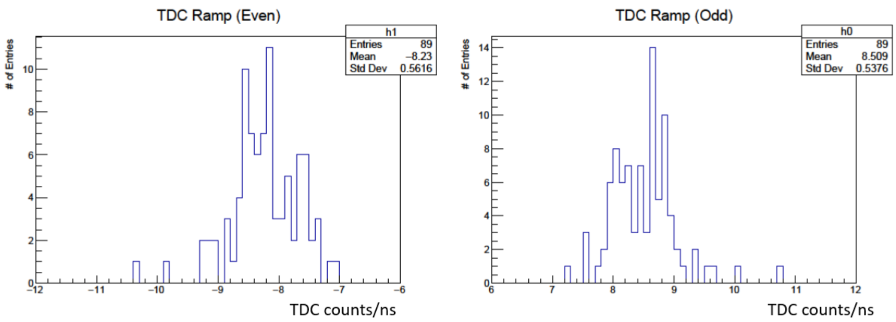

Figure 3.10: TDC ramp slopes of 89 ASUs.(left: ramp-down, BCID is even, left: ramp-up, BCID is odd)

3.4 Conclusion

We checked the performance of gain tuning and the threshold values corresponding to each photoelectron level ASU by ASU. The data of measured TDC ramp is used for the time calibration as described in Chapter 6. The tested 40 ASUs are installed to the upstream WAGASCI.

Chapter 4

Improvement of the DIF firmware

4.1 Introduction

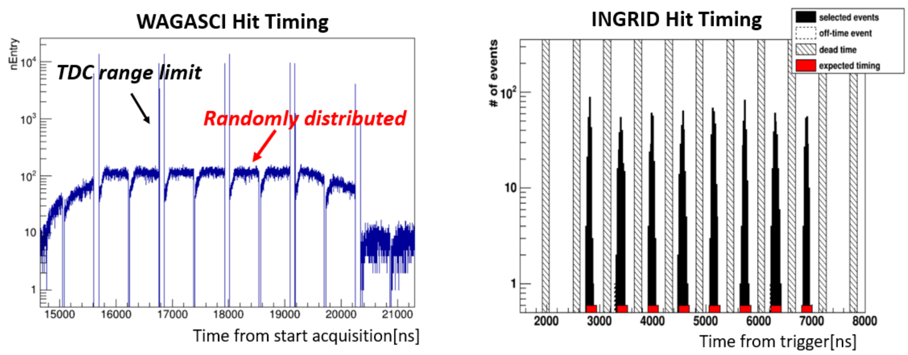

Figure 4.1: Hit timing distribution of WAGASCI(left) and that of INGRID (right) in the second pilot run.

We started to use the dedicated DAQ system since the second pilot run, but a problem with a timing measurement was revealed during the run. Figure 4.1 shows two hit timing distributions. That of a WAGASCI detector has randomly distributed regions. That of an INGRID detector shows eight peaks correspond to the T2K neutrino beam bunch structure(Figure 1.3,right).

In the WAGASCI electronics, the acquisition gate is opened synchronized to the beam trigger as explained in section 2.3.3. The system of timing measurement should also be synchronized to the beam trigger. The timing system is based on the slow clock as explained in section 2.3.3, but the slow clock was not found to be synchronized to the beam trigger so that a large timing jitter appeared in the timing measurement. In order to solve this problem, we cooperated with LLR and updated the firmware of DIF which controls the timing measurement system.

4.2 Test setup

In order to confirm the update of the DIF firmware and evaluate its performance, a test setup to inject a signal synchronized to an external trigger was constructed as shown in Figure 4.2. The external trigger for DAQ and a signal for light injection were made by a pulse generator. The light injection timing was adjusted by the gate generator module and the light yield was adjusted by the discriminator module. The adjusted signal was input to a blue LED and the light from LED was injected to a 32-channel arrayed MPPC. The LED and MPPC were fixed as shown in Figure 4.3 to reduce the change of conditions. The threshold of SPIROC was set to around 2.5 p.e. which is the same value as in the actual beam measurement. Thus some hits by dark noise are included in the following histograms, but they do not affect the discussion of the updated firmware.

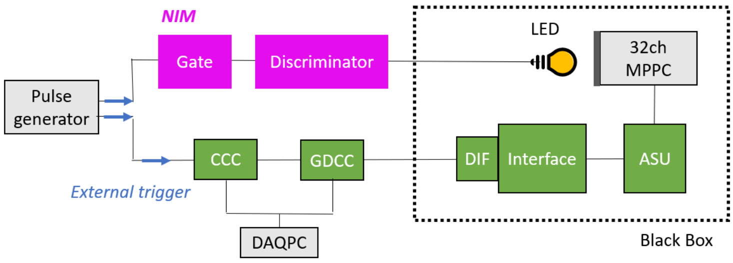

Figure 4.2: Overview of the test setup

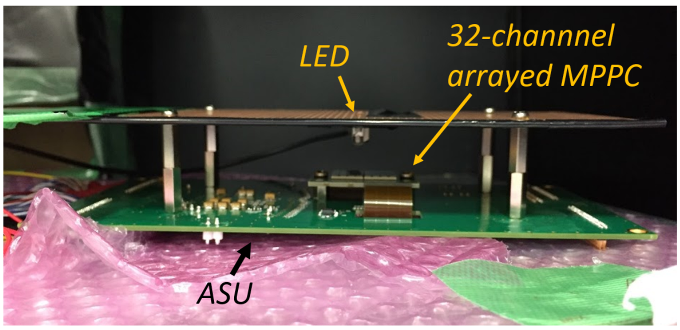

Figure 4.3: Picture of the light injection setup

Before the updates of the firmware, the performance of the original firmware was checked. The results are shown in Figure 4.4. The BCID values corresponding to the light injection timing are 7, 8, and 9. If the timing system is synchronized to the external trigger, the values should have only a value. Each TDC is randomly distributed and these histograms indicate the large timing jitter.

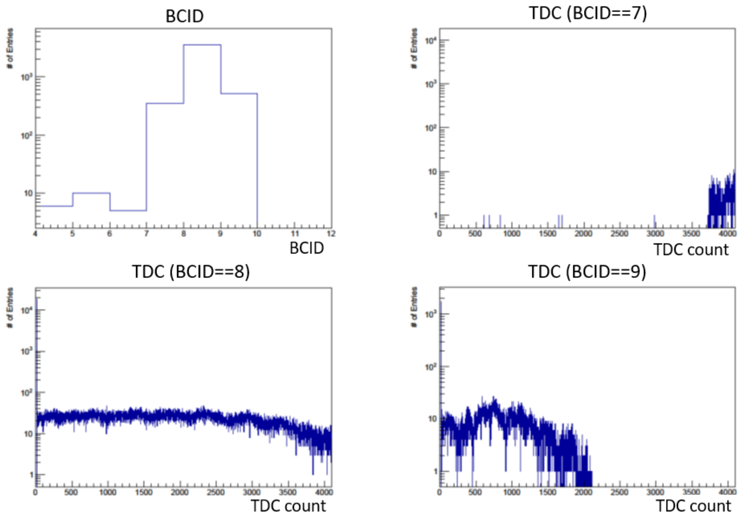

Figure 4.4: Results of the test with the original firmware

4.3 Update of the DIF firmware

4.3.1 Resetting the slow clock

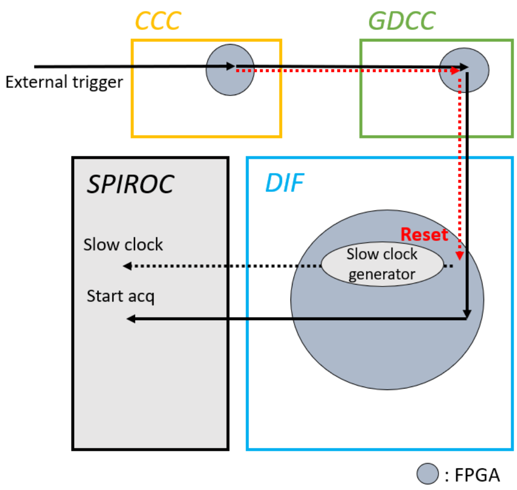

Figure 4.5: Schematic of the update by resetting the slow clock

First, we implemented a function to reset the slow clock when the DIF firmware receives an external trigger. A schematic of the update is shown in Figure 4.5. The external trigger passes through the FPGAs on CCC and GDCC and then the slow clock is reset in the DIF firmware. Figure 4.6 shows the results of the test with the updated firmware. The spread of the BCID distribution by the light injection is two and smaller than that of the original firmware. However each TDC is randomly distributed in the same way as the original firmware. The results indicate that the source of the timing jitter still remains.

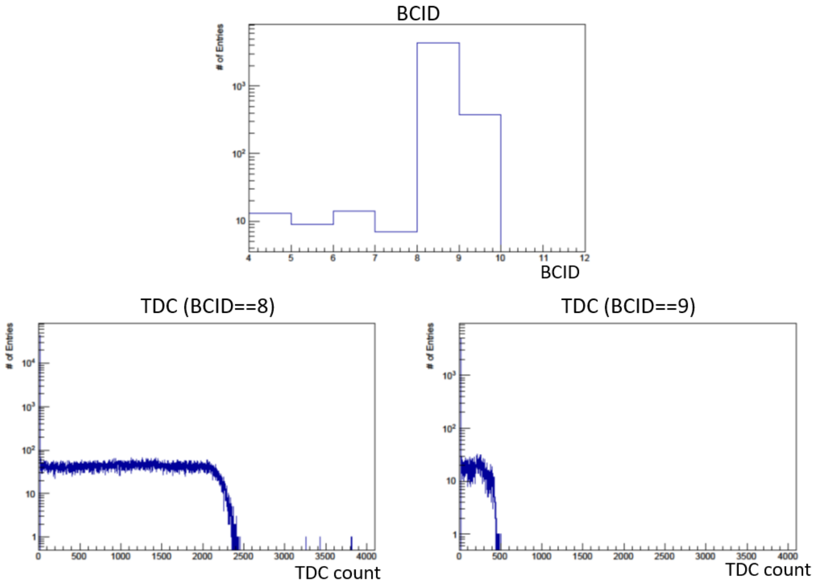

Figure 4.6: Results of the test with the slow clock reset

4.3.2 Direct path for reset signal

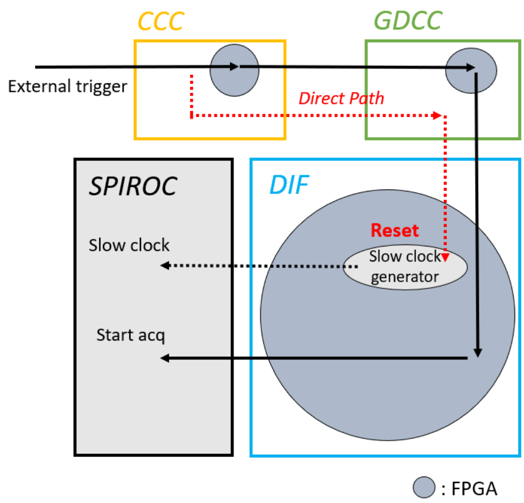

Figure 4.7: Schematic of the update by the direct path for reset signal

The remaining timing jitter came from the processing time in the FPGAs on CCC and GDCC. In this configuration, an external trigger is coded on 8 bits inside the CCC firmware and sent to GDCC. The GDCC firmware decodes the external trigger and sends a specific command to a coder function(8 bits/10 bits). The coded signal is sent to a decoder function(10 bits/ 8bits) in the DIF firmware and then the slow clock is reset by the decoded signal. This coding and decoding on the line explain the timing jitter and it corresponds to about 400ns.

In order to avoid the FPGAs, a direct path was utilized as shown in Figure 4.7. For the use of the path, a function to decode the external trigger directly was implemented in the DIF firmware. The path is used only for the signal to reset the slow clock.

Figure 4.8 shows the results of the test with the updated firmware. The spread of the BCID distribution by the light injection is two same as the previous update, but each TDC does not show the 400ns timing jitter.

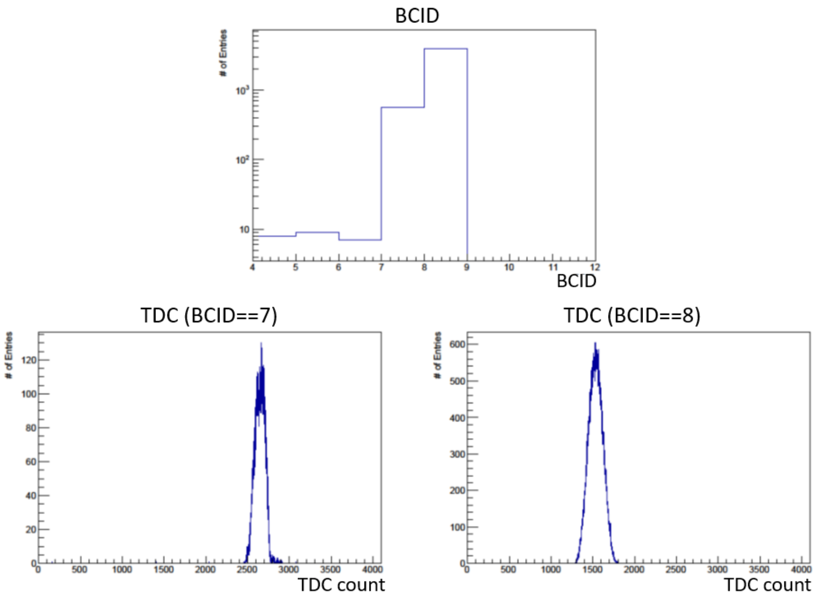

Figure 4.8: Results of the test with the direct reset path

The results can be explained in Figure 4.9. First, the external trigger passes through the direct path and arrives at the DIF firmware. Then it is detected by a fast clock with a period of 20ns and the slow clock is reset. Therefore the slow clock is synchronized to the external trigger by 20ns and the TDC distributions showed the effect of the synchronization. After a while, the trigger for the start-acq signal also arrives at the DIF firmware, but it still has the 400ns jitter. Because the start-acq signal is triggered by a rising edge of the slow clock after an arrival of the trigger, the timing shift of the start-acq signal is caused by the jitter. Thus the spread of the BCID distribution became two even if each TDC distribution was improved.

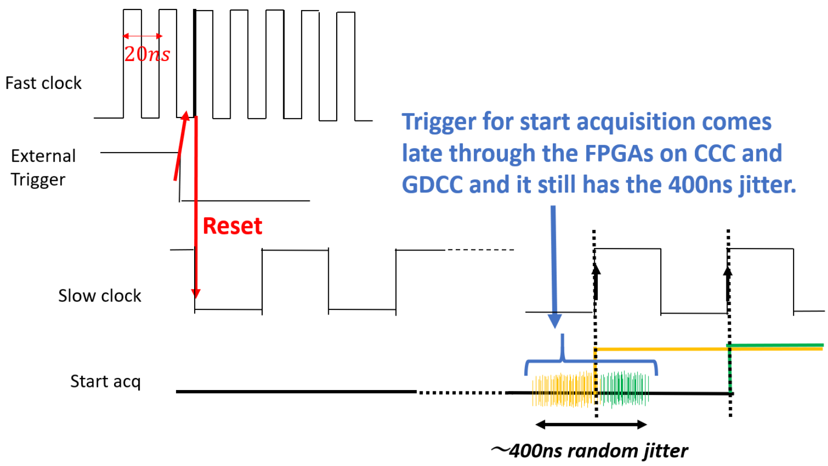

Figure 4.9: Chronogram of signals in the updated firmware(1)

4.3.3 Slow clock counter

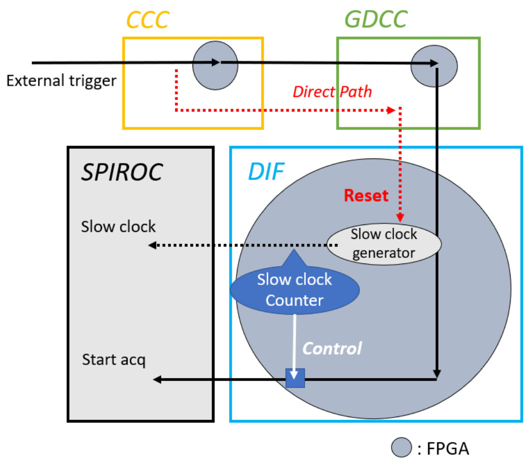

Figure 4.10: Schematic of the update by the slow clock counter

In order to avoid the timing shift, a counter of the slow clock was implemented as shown in Figure 4.10. The logic for the improvement by the counter is explained in Figure 4.11. As mentioned above, the trigger for the start-acq signal with the 400ns jitter arrives at the firmware after resetting the slow clock. The output of start-acq waits until the slow clock counter exceeds a certain number N. Figure 4.12 shows the change of the BCID values corresponding to the light injection timing when N changes. When N is two, the timing shift clearly appears. However when N becomes larger than two, the shift seems to be removed. According to this result, it is thought that the 400ns jitter should be on the border between the second clock and the third clock as shown in Figure

4.11.

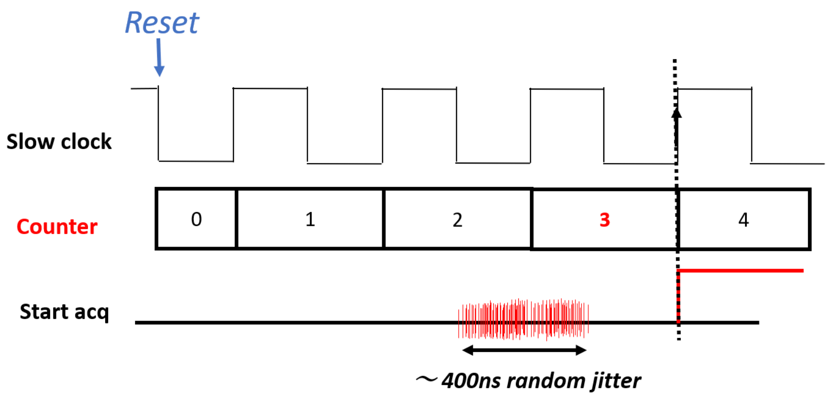

Figure 4.11: Chronogram of signals in the updated firmware(2)

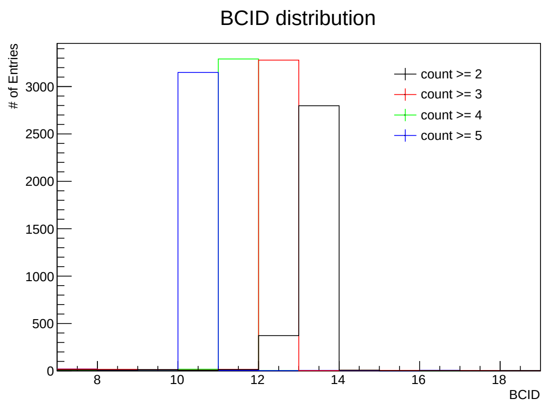

Figure 4.12: Change of the BCID values corresponding to the light injection timing

Regarding the implemented counter, a 5 bit jonson counter which changes 1 bit by 1 bit was applied. The jonson counter avoids that two or more bits change at the same time and removes an error source. Figure 4.13 shows the results of the test with the updated firmware. TDC distribution with BCID=12 indicates that a few shifts still remain even though the situation gets better thanks to the implemented counter.

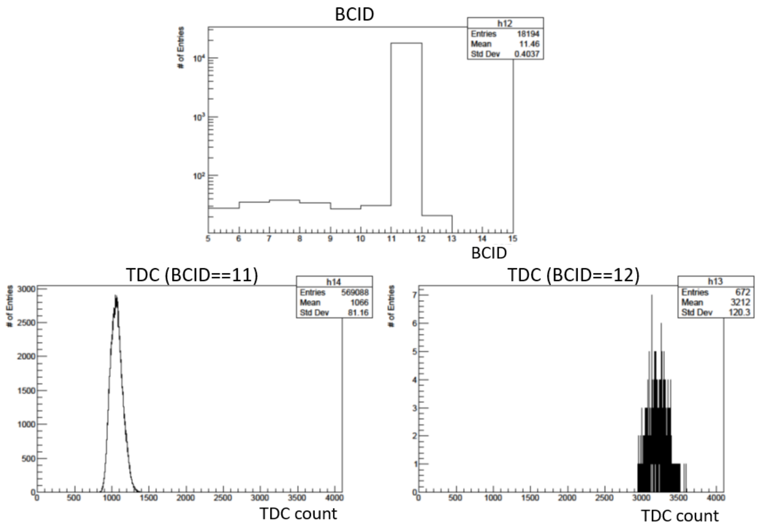

Figure 4.13: Results of the test with the slow clock counter

4.3.4 Adjustment of count timing

Because the implemented counter seemed to work well as shown in Figure 4.12, the timing to reset the slow clock was suspected. Figure 4.14 shows how the slow clock is generated and reset in the DIF firmware. The fast clock is generated in CCC and sent to each DIF. The DIF firmware counts the number of the fast clock. When the number is 0 to 14, the firmware makes a low level signal. When the number is 14 to 28, the firmware makes a high level signal. These continuous signals are realized as the slow clock with 580ns period. The reset function implemented in the firmware update sets the fast clock count to 0 when the firmware receives the external trigger.

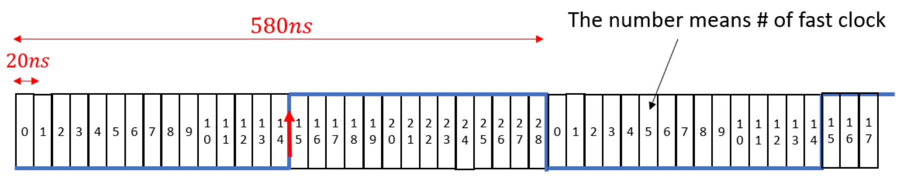

Figure 4.14: Generation of the slow clock

At this point, the timing to start counting the slow clock is earlier than the timing to reset it by 40ns as shown in Figure 4.15. The time gap is so small that some crashes should occur and it is better to start counting the slow clock after resetting it. Therefore the count timing was delayed by 60ns. The timing chart of the update is shown in Figure 4.16. Figure 4.17 shows the results of the test with the updated firmware. As the histograms show, the shift was completely removed and the firmware update was successful.

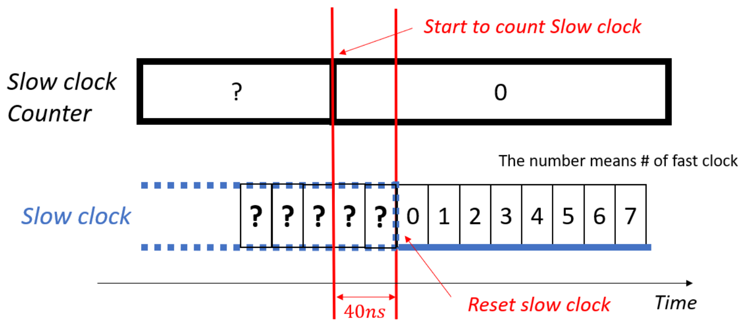

Figure 4.15: Time gap between resetting the slow clock and counting it

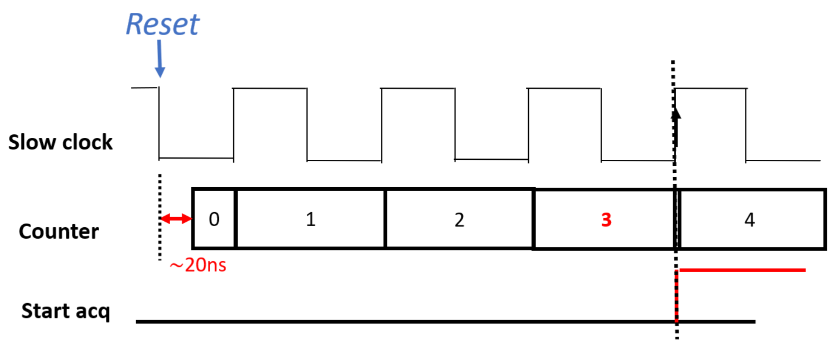

Figure 4.16: Chronogram of signals in the updated firmware(3)

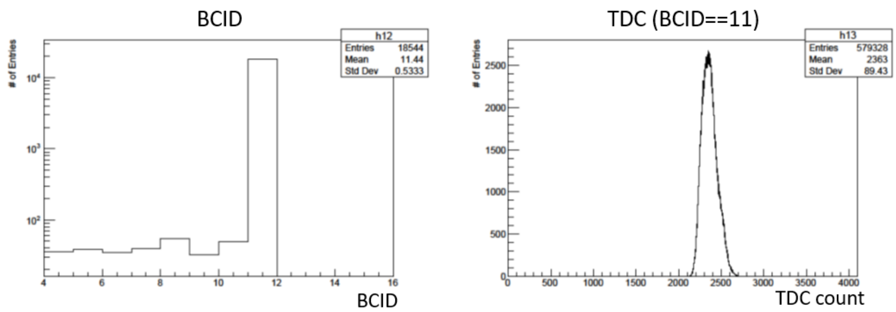

Figure 4.17: Results of the test with the updated firmware

4.4 Summary

The added functions to solve the problem are as follows;

1. Reset the slow clock when the firmware receives the external trigger

2. Decode the external trigger directly in order to utilize the direct path for the signal to reset the slow clock
3. Implement the slow clock counter
4. Delay the timing to start counting the slow clock

The updated firmware have been applied since the first physics run.

Chapter 5

Status of the physics run

We started the first physics run in November 2019. The data taking is scheduled until February 2020. The status of the data taking by the end of 2019 is explained in this chapter.

5.1 Accumulated POT

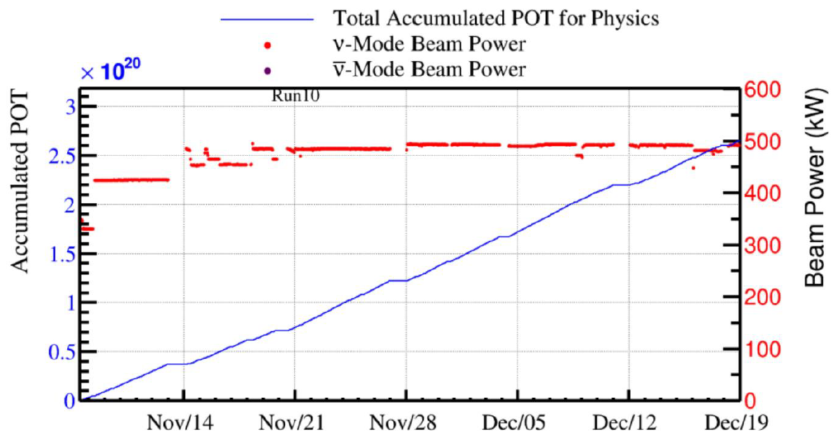

Figure 5.1: Accumulated P.O.T(7 Nov. 2019 - 19 Dec. 2019)

Figure 5.1 shows the accumulated number of protons on target(P.O.T) for the T2K experiment. The total P.O.T for this period is 2.65×10^{20}. In the whole period, we continued to take data with all detector modules of the T2K-WAGASCI. Therefore the number is almost consistent with that for WAGASCI although we had some DAQ troubles.

5.2 Beam bunch structure

Figure 5.2 shows the hit timings of the WAGASCI detector. The eight peaks indicate the resconstruction of the beam bunch structure. We confirmed that the timing measurement system is synchronized to the beam trigger thanks to the updated DIF firmware(Chapter 4). We adjusted the acquisition gate to match the beam timing to the valid TDC range. The detail is explained in Appendix B.

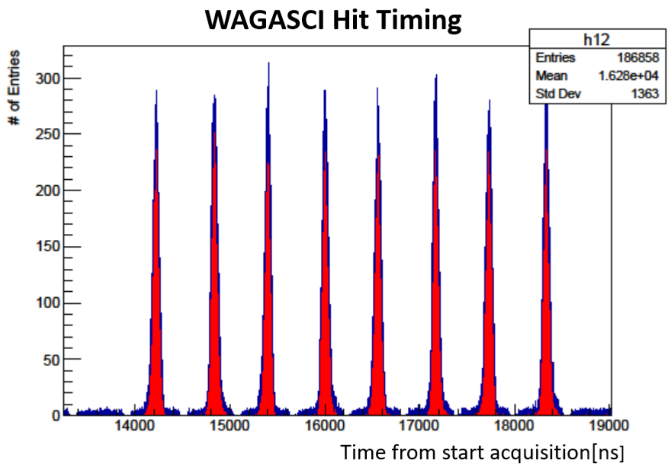

Figure 5.2: Hit timing distribution of the WAGASCI detector in the first physics run

5.3 Event matching

WAGASCI-WallMRD, BabyMIND and Proton Module are operated by independent DAQ systems. In order to check these systems properly, we check event matchings between the modules. Various events are observed by track matching. We confirmed that we can synchronize events recorded by different systems offline by looking at eveny displays. The procedure is as follows;

1. Track reconstruction for each detector
2. Spill number matching

   Spill information from the J-PARC beam line is recorded by each system. We check the spill number between modules.
3. Bunch matching

   We check the time of event for each detector. The time measurement systems are different for each DAQ system. For example, the WAGASCI DAQ measures time from the start acquisition, while the BabyMIND DAQ system measures time from the beam trigger as shown Figure 5.3. We require the event to be in the same bunch.
4. Track matching with event display

   We check whether each track is connected between the modules. The examples of the event display are shown in Figure 5.4 and 5.5.

We confirmed that we can synchronize WAGASCI, BabyMIND and Proton Module, although WallMRD had a problem explained in the following section.

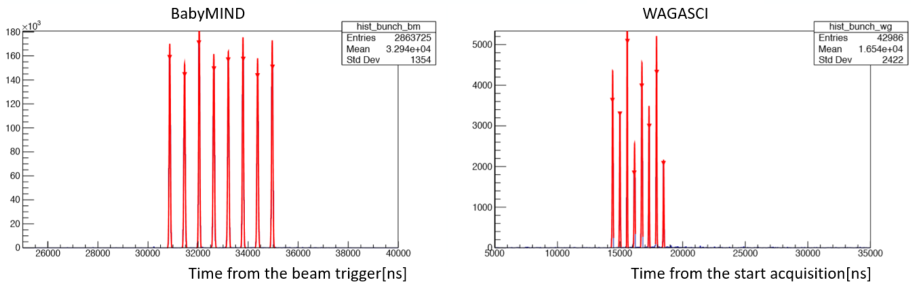

Figure 5.3: Hit timing distribution for BabyMIND(left) and WAGASCI(right)

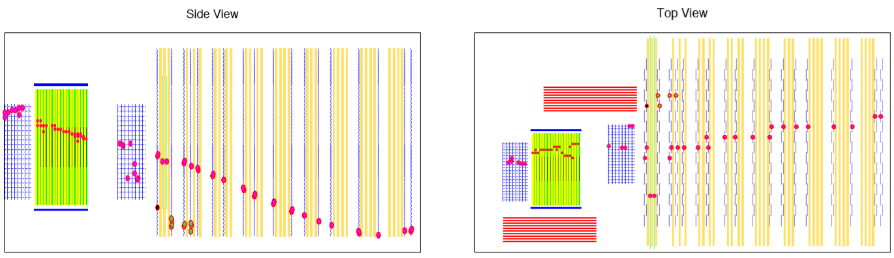

Figure 5.4: Example of events in a spill with all detectors(1). The difference of color means that of bunch.

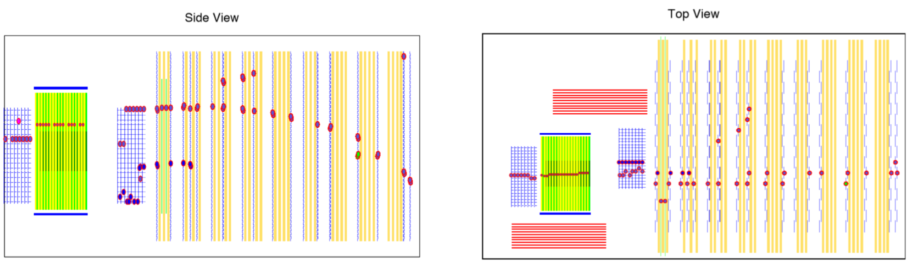

Figure 5.5: Example of events in a spill with all detectors(2). The difference of color means that of bunch.

5.4 Noise problem in WallMRD

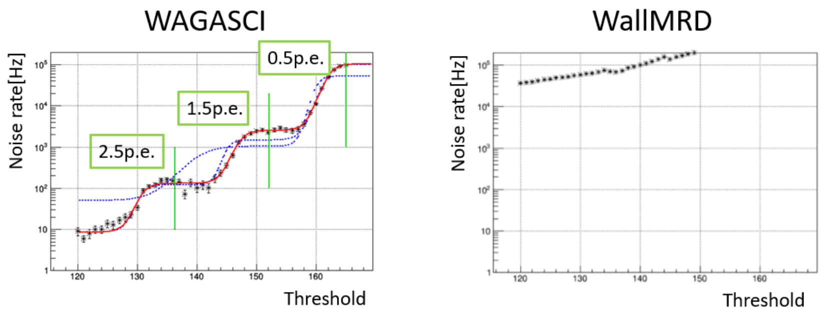

Figure 5.6: Examples of threshold curve measurement (left: WAGASCI, right: WallMRD). The plot of WallMRD does not show clear photoelectron structure because of large noise.

The WallMRD had a problem due to a large noise. Figure 5.6 shows the plots of the threshold curve measurement with WAGASCI and WallMRD. The plot for WAGASCI shows the threshold curve as discussed in section 3.2. However that for WallMRD does not show clear photoelectron structure because of large noise. It is found that the charge information corresponding to the noise hits is of the pedestal level. It indicates the exsistence of noise in the trigger part. We have investigated the problem but we have not found solution by the end of 2019. The detail of the problem is discussed in Appendix C.

Chapter 6

Time calibration of the WAGASCI detector

6.1 Introduction

We record hit timing information as BCID and TDC. The latter gives us a fine time information. In order to convert TDC count to the real time, we must know two parameters, a slope and an intercept. The slopes were measured so that we need to adjust origins for each ASU. In addition, a time walk effect of SPIROC2D should also be corrected. We calibrated the time measurement system of the WAGASCI detector with following steps.

1. Calibrate the timing difference of ASUs lined up along the beam direction
2. Calibrate the timing difference of ASUs lined up along the direction perpendicular to the beam
3. Correct the time walk effect

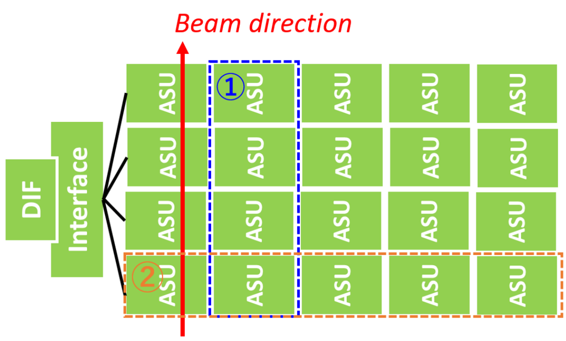

Figure 6.1: ASU arrangement of the WAGASCI detector

6.2 Calibration along the beam direction

6.2.1 Analysis data

In order to calibrate the difference of ASUs lined up along the beam direction, we used the neutrino beam data of the physics run. In many cases, neutrinos interact with the wall in front of the WAGASCI location and the forward scattered muons penetrate the detector modules as shown in Figure 6.2. The two WAGASCI detectors were used to select the single muon track. We used the following event cuts to select the event.

1. Time clustering

   Hits of each detector were clustered by their hit timings. 10 hits or more were required within 100ns to start clustering by the hit timing. All the hits within 50ns from the average time were classified into a cluster. When hits of both WAGASCI detectors were clustered by the time clustering, the event was selected. This event cut is useful to reduce random MPPC noise hits.

2. Passing area cut

   Figure 6.3 explains this event cut. When all the hits of track was in a defined area, the event was selected. The area was within the 30 $cm \times 30$ cm transverse area in the WAGASCI detector. The center of the area was not specified. When both WAGASCI detectors met this condition, the event was selected. This event cut is useful to select a single track event.

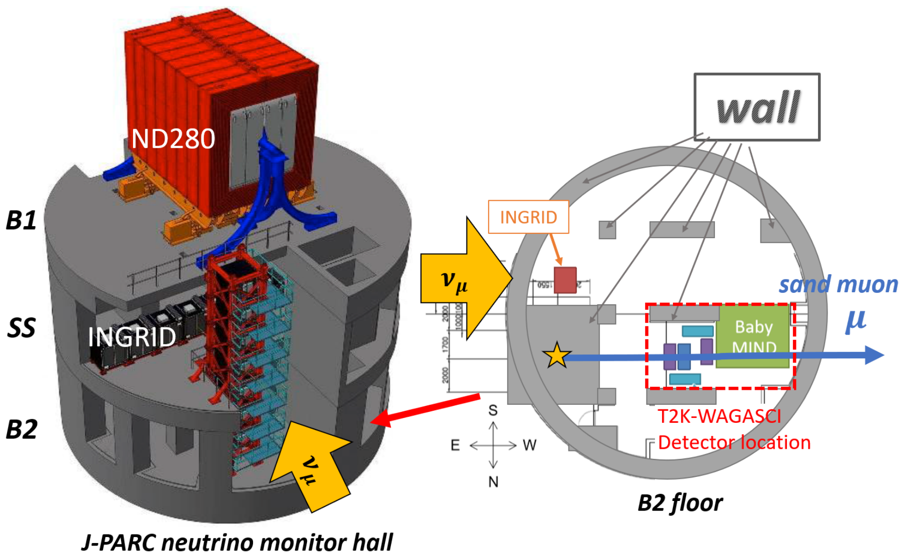

Figure 6.2: Explanation of the sand muon. The T2K-WAGASCI detectors are located on the B2 floor of the J-PARC neutrino monitor hall. Neutrinos often interact with walls surrounding the detectors and generate muons called sand muons.

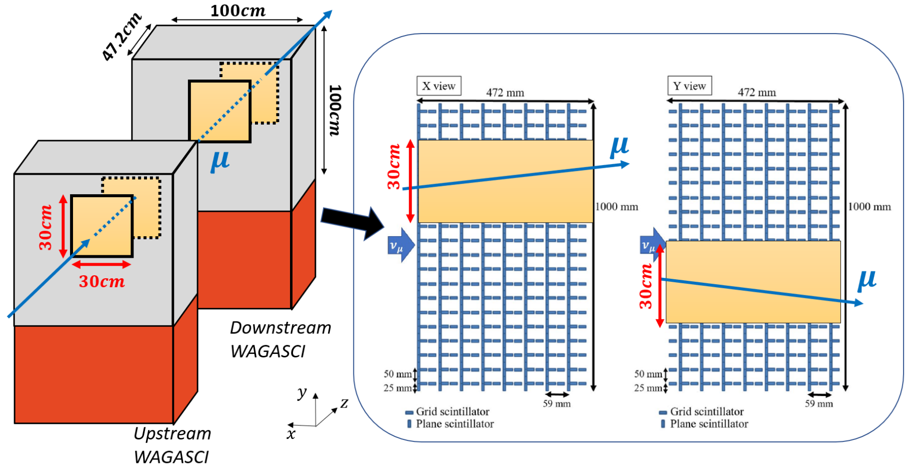

Figure 6.3: Explanation of the passing area cut

6.2.2 Calibration

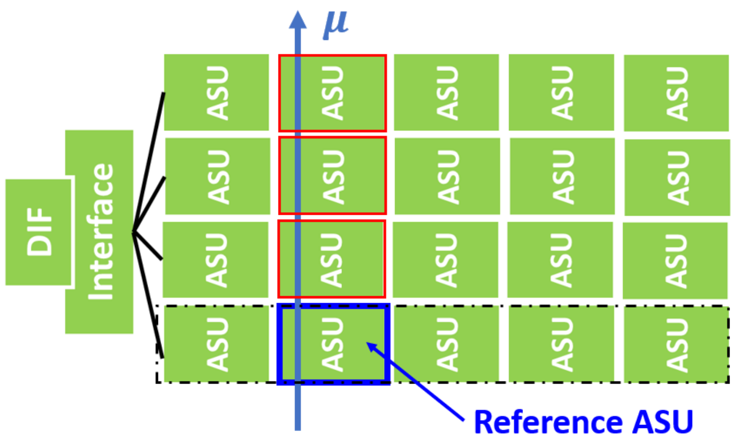

Figure 6.4: Overview of the calibration and its exepected result

We compared the hit times of each ASU on the same horizontal line as shown in Figure 6.4. The moset upstream ASU is chosen as a reference for each line. We checked hit time differences between the reference ASU and the other ASUs on the line as shown in Figure 6.5. The measured slopes were applied to each ASU and a common intercept was appllied to all the ASUs for this histogram. The time difference should be small, but the differences are largely distributed. Examples of two ASUs are shown in Figure 6.6. They show distributions of hit times from the mean of the reference ASU, but they are colored for each BCID. In the case of the left plot(case1), the histogram of BCID with odd(red) is shifted to negative and that of BCID with even(blue) is shifted to positive. The right plot(case2) has the opposite way.

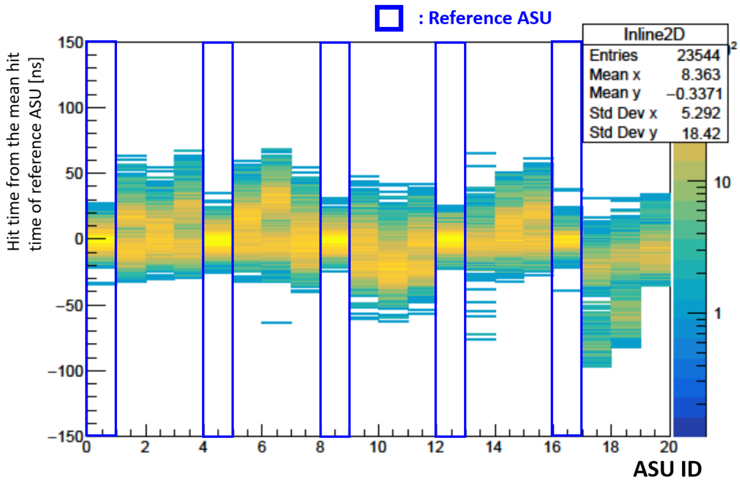

Figure 6.5: Hit times from the mean of the reference ASU. The blue frames show distributions of the reference ASUs. Two peaks appear in many cases.

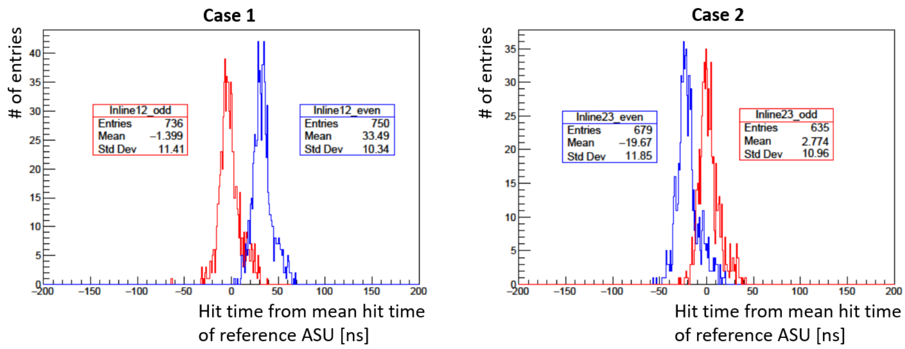

Figure 6.6: Two examples of the hit time distribution from the mean of the reference ASU. (red: BCID is odd, blue: BCID is even)

Figure 6.7 explains this result. According to Figure 3.10, the slopes of each BCID seem to be symmetric. In the case1(led line), the calculate time (t_{case1}) is smaller than the expected time(t) in the histogram of BCID with odd. In addition, the calculated time is larger than the expected time in the histogram of BCID with even. Thus the time difference($t_{case1} - t$) should be different for each BCID. The case2(blue line) is explained in the same way. Therefore, this result indicates the necessity of the time origin adjustment for each ASU.

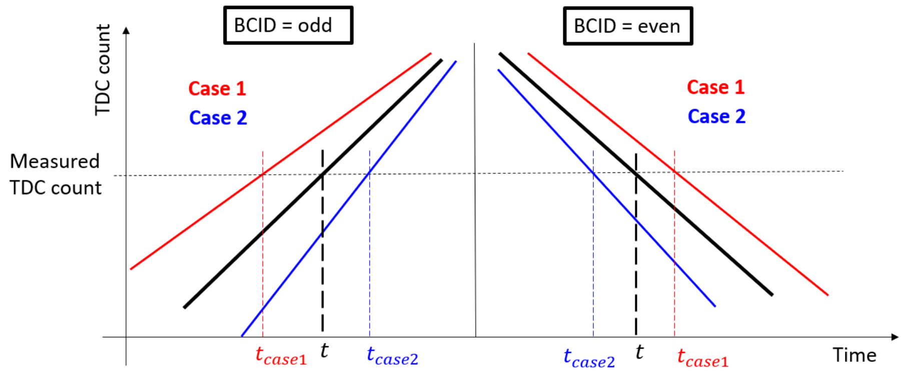

Figure 6.7: Explanation of the two peaks. Case1 corresponds to the left histogram and Case2 corresponds to the right histogram in Figure 6.6.

We adjusted the origins by choosing appropriate intercepts for each ASU. The intercepts are optimized based on the hit time of the reference ASU. The method is explained in Figure 6.8. We corrected the time gap between a calculated hit timing and an expected one by adjusting an intercept. The expected timing was defined with the hit timing of the reference ASU. It included the little effect of the distance between ASUs corresponding to 12cm. We calculated the adjusted intercept event by event. Figure 6.8(right) shows the distribution of the calculated intercept of an ASU of BCID with odd. We used the mean of the distribution as a calibrated intercept.

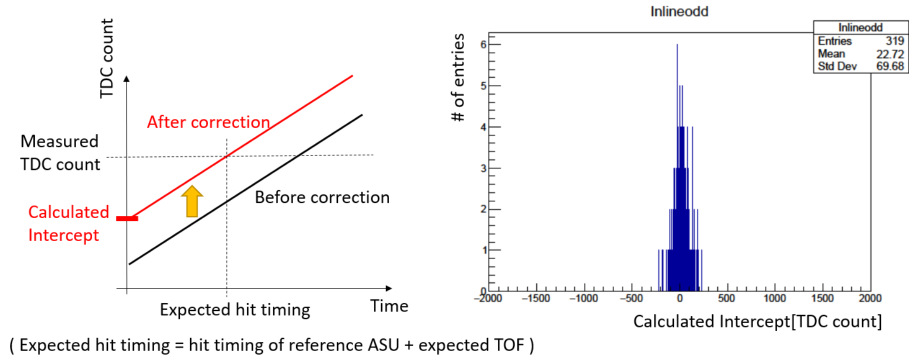

Figure 6.8: Calculation of the TDC ramp intercept. The right histogram is an example of distribution of the calculated intercept. The mean of the distribution was applied as an intercept of the TDC ramp.

The beam data was analyzed again with the calibrated intercepts. The result is shown in Figure 6.9. The distributions of each ASU concentrate on zero compared with Figure 6.5 and we can see that the time gap was calibrated correctly.

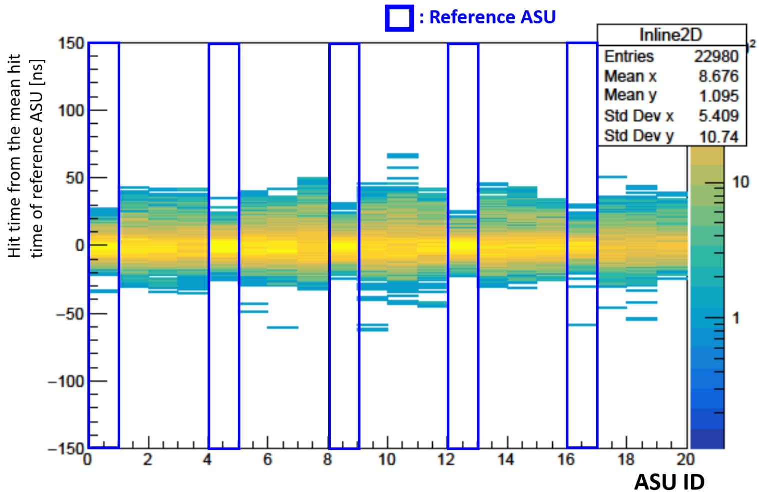

Figure 6.9: Result of the calibration. It shows hit times from the mean of the reference ASU.

6.3 Calibration along the direction perpendicular to the beam

6.3.1 Analysis data

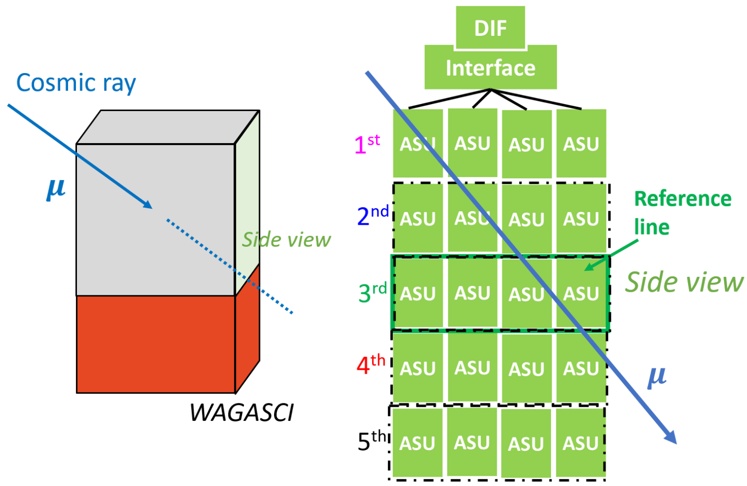

Figure 6.10: Overview of the calibration and data for the calibration.

In order to calibrate the difference of ASUs lined up along the direction perpendicular to the beam, we used cosmic data. The passing area cut is not suitable for the cosmic data, so that we used the different event cuts as below;

1. Time clustering

This event cut was same as above, but it was applied for each view. The reason is because we often have events in which a muon falls vertically. This kind of event is rejected when this event cut is applied to both views simultaneously.

2. Track fitting

   We fitted hit positions by a linear function for each event. The width of the scintillator(2.5cm) was appllied to error bars for each axsis as shown in Figure 6.11. Events were selected by putting restraint on the p value. The p value of the selected event was larger than 0.1 and smaller than 0.9.

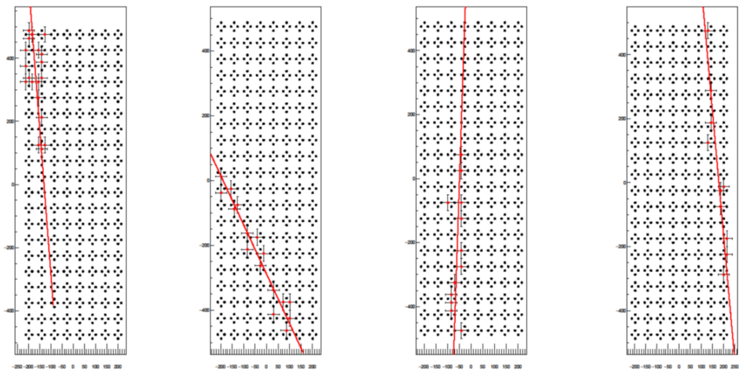

Figure 6.11: Examples of the event display. The error bars correspond to the width of the WAGASCI scintillator.

6.3.2 Calibration

Because we already calibrated the difference between the ASUs on a horizontal line, we used the mean hit times for each horizontal line. The differences of the mean hit times between the adjacent lines were checked for each BCID as shown in Figure 6.12. The plots indicate the timing system is not synchronized between lines. It should be noted that this result includes the effects of not only the asynchronization between lines but also the transportation time of the start-acq signal which is discussed in Appendix D.

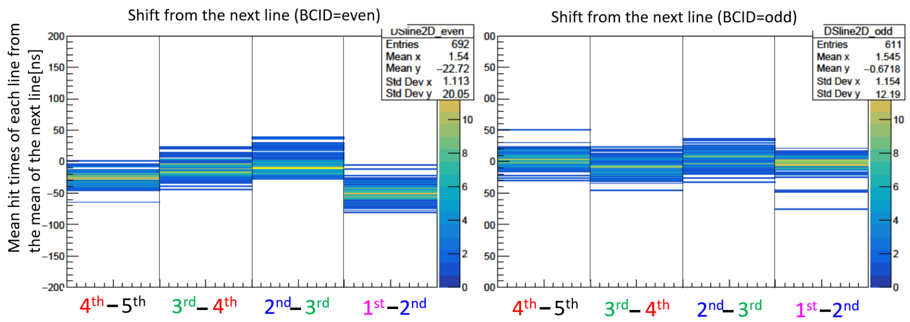

Figure 6.12: Differences of the mean hit times between the adjacent lines. (before the calibration)

In order to calibrate the difference between lines, the center line was chosen as a reference as shown in Figure 6.10. We adjusted the time origin for each line to that for the reference. Distributions of each line were fiited by a gaussian function and we shifted the time origin by its mean value. Figure 6.13 shows the result of the calibration. Thus the whole system was synchronized by the two calibrations.

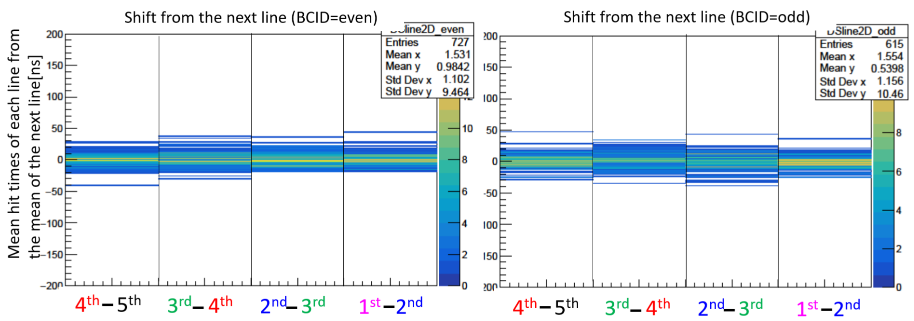

Figure 6.13: Differences of the mean hit times between the adjacent lines. (after the calibration)

6.4 Time walk correction

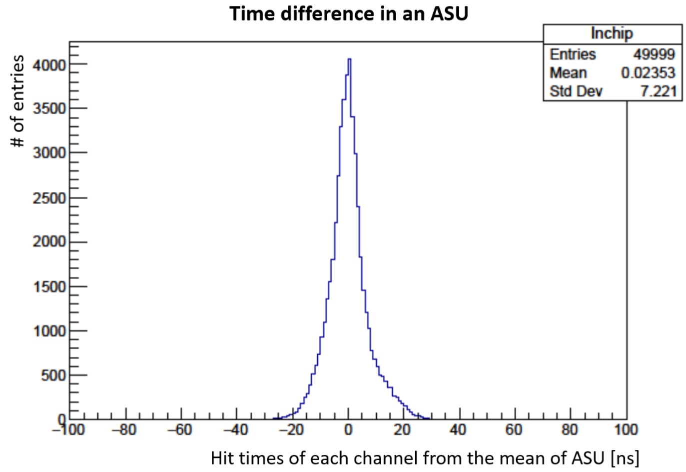

Figure 6.14: Hit time differences between the mean hit time of an ASU and hit times of each channel in the ASU

Figure 6.14 shows the hit time differences between the mean hit time of an ASU and hit times of each channel of the ASU. These are calculated from the neutrino beam data for the calibration discussed in section 6.2. The two calibrations were considered in this histogram. The standard deviation is 7.2 ns and we wanted to improve this result. We focused on a time walk effect as one of the timing jitters. In order to check it, we added the charge information to the histogram as shown in Figure 6.15(left). We can see a correlation between charge and hit time. When charge is small(under 700 ADC count), the hit times from the mean get earlier in proportion to charge. When charge is large(over 1000 ADC count), the hit times from the mean get delayed in proportion to charge. This correlation is explained by the time walk effect.

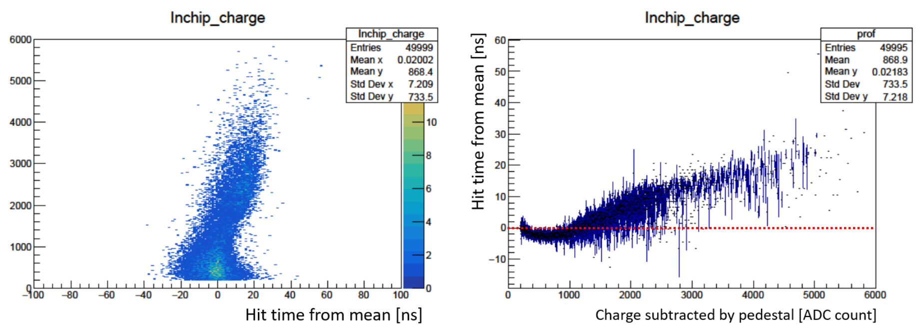

Figure 6.15: Correlation between charge and hit timing(left). This plot was made by adding the charge information to the histogram in Figure 6.14. Mean time corresponding to each ADC count(right).

In the case of SPIROC2D, two kinds of time walk have been observed. The trigger timing is determined by the fast shaper signal and threshold. One is that the trigger timing gets earlier when charge gets larger as illustrated in Figure 6.16. This time walk has large effect when charge is small. The other is that the trigger timing gets delayed when charge gets larger as illustrated in Figure 6.17. The fast shaper gets saturated so that the trigger timing is delayed in proportion to charge. This time walk has large effect when charge is large. This effect is particular to SPIROC2D becuase of the threshold problem explained in section 2.3.3.

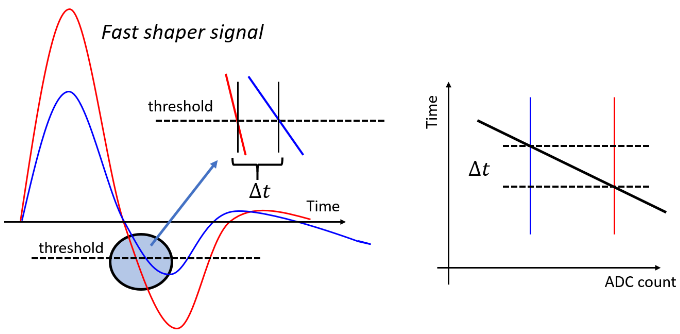

Figure 6.16: One of the time walk effects(1). The trigger timing gets earlier in proportion to charge. This time walk has large effect when charge is small.

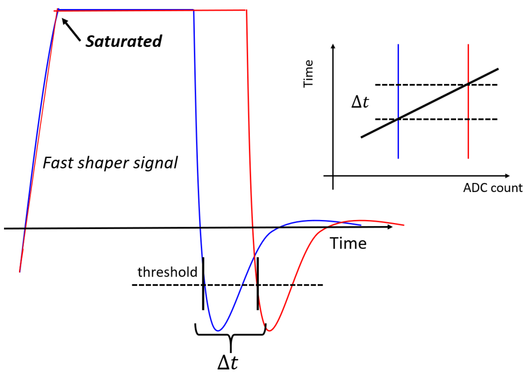

Figure 6.17: One of the time walk effects(2). The trigger timing gets delayed in proportion to charge. This time walk has large effect when an injected charge is large.

In order to correct the time walk, the mean time of the two dimensional histogram was projected for each ADC count as shown in Figure 6.15(right). When charge is small (up to 1000 ADC count), we corrected the time gap from the expected time for each ADC count. When charge is large (over 1000 ADC count), we corrected it by a linear fitting. The corrected result is shown in Figure 6.18 and 6.19. The standard deviation was improved from 7.2ns to 5.8ns.

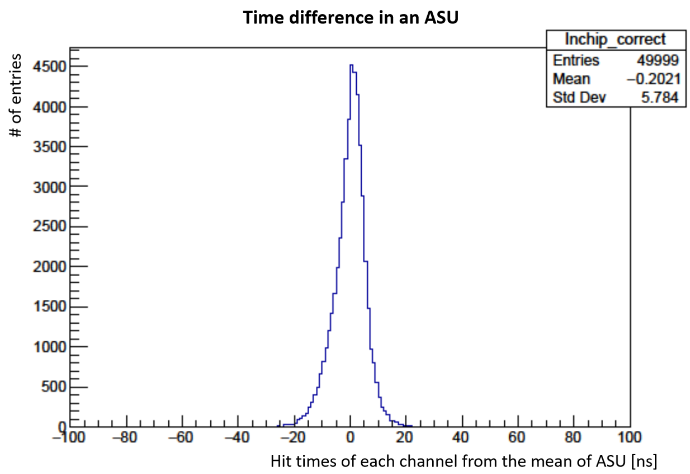

Figure 6.18: Hit time differences between the mean hit time of an ASU and hit times of each channel of the ASU after the time walk correction

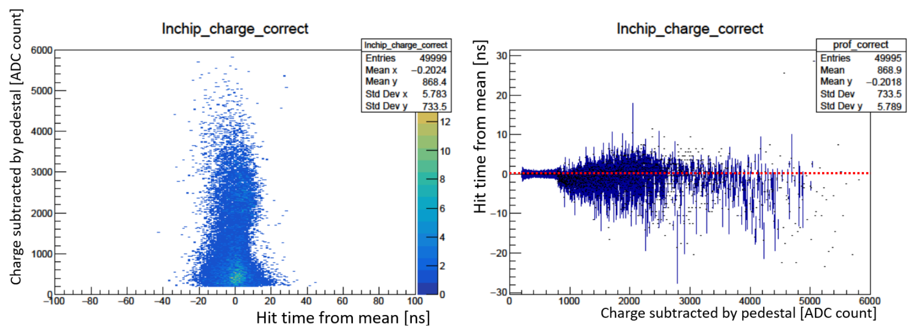

Figure 6.19: Correlation between charge and hit timing(left) and mean times corresponding to each ADC count(right) after the time walk correction

6.5 Evaluation

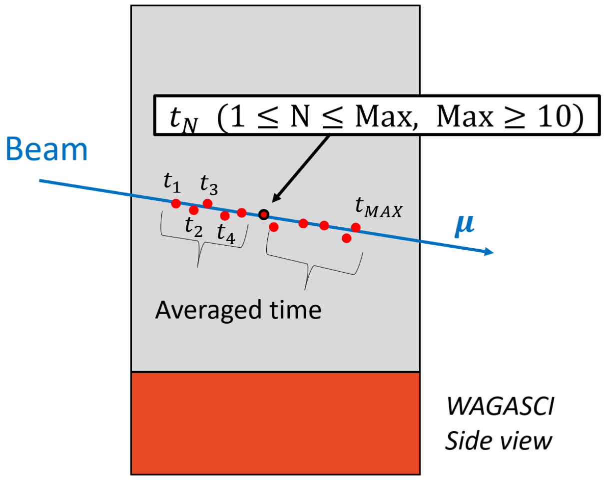

Figure 6.20: Method to estimate the timing resolution per one channel

In order to evaluate the timing performance of the WAGASCI detector, we estimated the timing resolution per one channel. The neutrino beam data explained in section 6.2 was used for the estimation. A hit was selected randomly for each event. The differences between its hit time and the averaged hit time of the other hits were caluculated as described in Figure 6.20. When we request ten or more hits for the calculation, the errors of the averaged time are suppressed considerably.

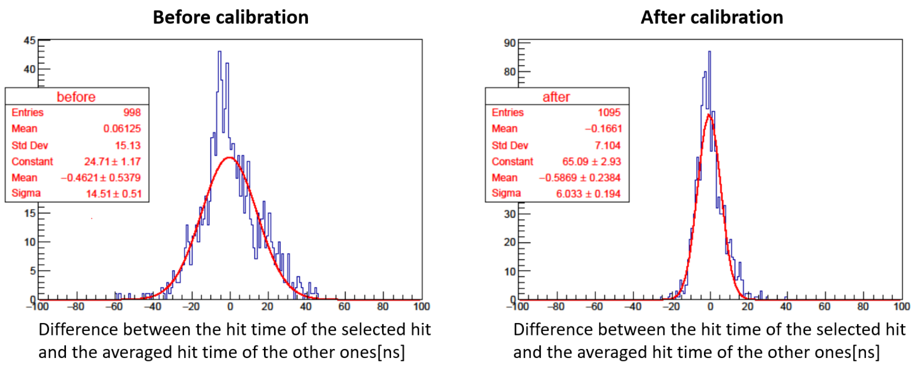

Figure 6.21: Difference between the hit time of the selected hit and the averaged time of the other ones (left: before the calibration, right: after the calibration)

Figure 6.21 shows the distributions of the time difference. Both calibrated data and noncalibrated data were checked. Their timing resolutions were estimated by gaussian fitting. The result is summarized in Table 6.1.

	Before calibration	After calibration
Timing resolution [ns]	15 ± 1	6.0 ± 0.2

Table 6.1: Timing resolution of the WAGASCI detector

6.6 Conclusion

We calibrated the time measurement system of the WAGASCI detector. The calibration improved the timing resolution from 15 ns to 6.0 ns. However this result is inferior to that of the timing resolution measurement discussed in section 2.3.4. Therefore, we need to improve the time calibration.

Chapter 7

Background rejection using timing information

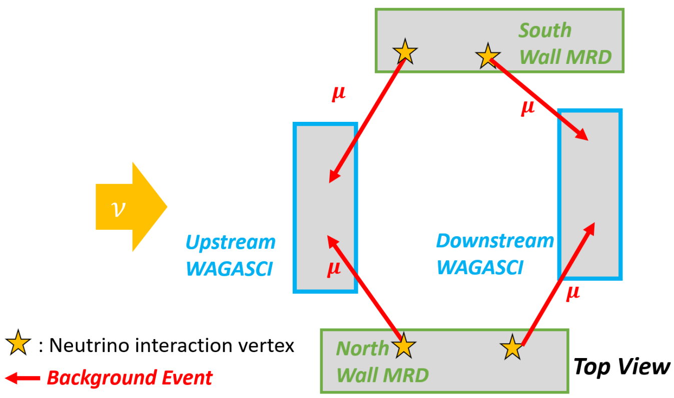

Figure 7.1: Background event from WallMRD

The WallMRD detectors are used to identify muons generated by neutrino interaction in the WAGASCI detectors. However they can become a source of background event as shown in Figure 7.1, if we cannot identify the direction of particles. There is a high chance that a neutrino interacts with a WallMRD detector because of its large mass($\sim$ 8.5 tonne). We evaluate the feasibility of background rejection based on the timing information. First, the event rate is estimated using a Monte Carlo simulation. Then, the background rejection method is developed and the performance is evaluated assuming that the expected timing resolutions are realized.

7.1 Event rate estimation

A Monte Carlo simulation which reproduces the T2K-WAGASCI was used for this study. The simulation consists of three independent softwares. Firstly JNUBEAM [21] which is a software to reproduce the T2K neutrino beam is run. It simulates interactions of incident 30 GeV proton and carbon target, behaviors of the secondary particles and decays of the pion and kaon in the decay volume which predicts the neutrino flux at the experimental site. Then NEUT[22] which is a software to reproduce a neutrino interaction is run. It simulates a neutrino interaction with a nucleus of detector, including final state interactions inside the nucleus. Finally, Geant4 which reproduces the T2K-WAGASCI detector configuration (Figure 7.2) is run. It simulates behaviors of the secondary particles in the detector and calculate energy deposits in the plastic scintillators.

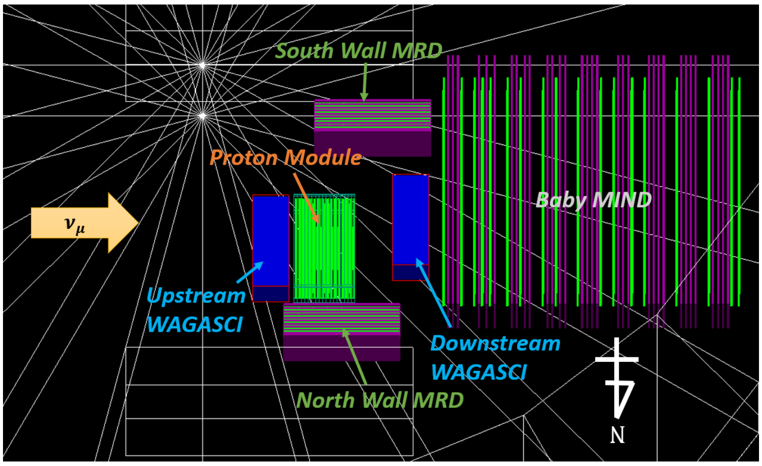

Figure 7.2: View of the T2K-WAGASCI detector configuration reproduced by Geant4

7.1.1 Definitions of signal event and background event

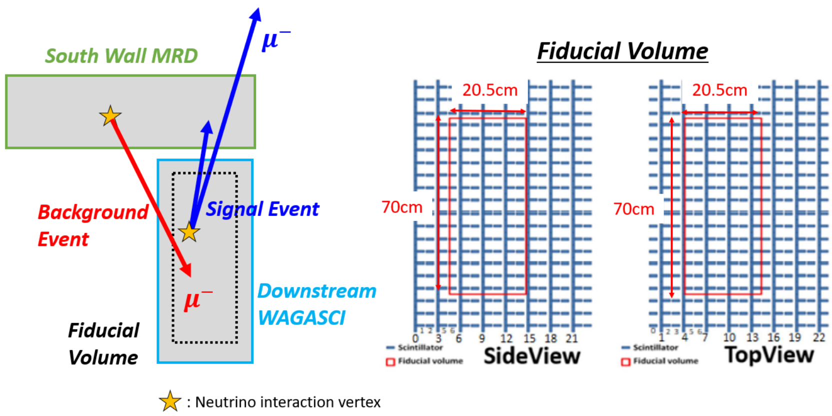

Figure 7.3: Definitions of the signal event, the background event(left) and the fiducial volume of the WAGASCI detector(left)

We simulated the signal events generated in the WAGASCI detector and the background events in WallMRD. For the signal events, the neutrino interaction vertex is requested to be inside the fiducial volume shown in Figure 7.3(right). The fiducial volume is the region

- between the 5th tracking plane and 14th one along z-axis, and
- within the central 70 $cm \times 70$ cm transverse area

For the background events, the muon generated in the neutrino interaction inside WallMRD is required to stop inside the fiducial volume of a WAGASCI detector. Time clustering (section 6.2) is applied for both signal and background events. We requested three or more hits to start clustering for each detector.

7.1.2 Estimated event rate

	Signal event	**Background event**
Total	76.2%	23.8 %
	(2680 events)	(839 events)
Up WG - South WMRD	26.1 %	0.0316 %
	(917 events)	(1 event)
Up WG - North WMRD	43.0 %	0.00 %
	(1515 events)	(0 event)
Down WG - South WMRD	**5.30** %	**23.6** %
	(**186 events**)	(**829 events**)
Down WG - North WMRD	1.75 %	0.247 %
	(62 events)	(9 events)

Table 7.1: Result of the event rate estimation. The numbers in the parentheses are the expected number of events for 5.0×10^{21} POT.

Table 7.1 shows the event rates of each case and the expected number of events for 5.0×10^{21} POT. The background from the south WallMRD to the downstream WAGASCI is found to be significant. In order to utilize the south WallMRD and keep the acceptance for the large angle muons from the downstream WAGASCI, background rejection is necessary.

Figure 7.4 shows the number of hits and the path length of background muons. The mean hit number of the WAGASCI and that of the WallMRD are 12 and 5, respectively, and the mean path length is 144 cm. We would like to discriminate the two possible directions of tracks. The average time difference between two cases over the average path length is 144cm*2/c = 9.6ns. Thus, the direction identification should be possible with a hit timing resolution of a few ns.

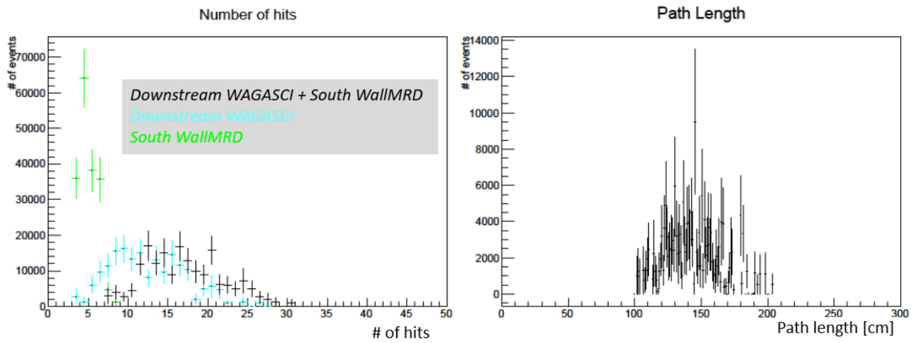

Figure 7.4: Information of background events between the downstream WAGASCI and the south WallMRD. (left: number of hits a muon leaves in each detector, right: path length of muon)

7.2 Evaluation

We have evaluated the background rejection capability using the Monte Carlo simulation. The result of the timing resolution measurement discussed in section 2.3.4 was implemented to each detector in the simulation.

7.2.1 Analysis

We have tried two methods to identify the muon direction by hit times.

Analysis method1

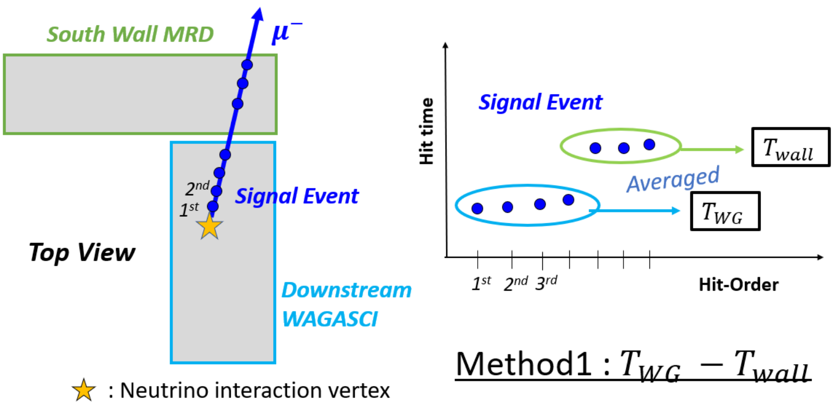

Figure 7.5: Overview of the analysis method1.

We can identify the muon direction by the hit timing difference between the WAGASCI and the WallMRD. The hit timings in a cluster are averaged for each detector and the averaged hit timings were represented by T_{WG} and T_{wall}. We used $T_{WG} - T_{wall}$ to discriminate the signal and background events. Figure

7.5 explains this analysis method by giving an example of the signal event. A signal (background) event has negative (positive) $T_{WG} - T_{wall}$.

Analysis method2

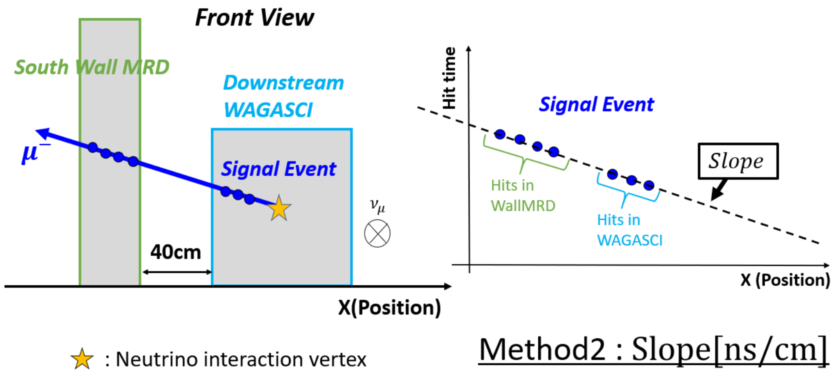

Figure 7.6: Overview of the analysis method2.

We can identify the muon direction by a slope which is calculated by hit positions and hit times. If we make a graph of the relationship between hit times and hit positions of the horizontal axis from the view of the neutrino beam, a slope should appear as shown in Figure 7.6. We used the slope value which is calculated by a linear fitting to discriminate the signal and background events. Figure 7.6 explains this analysis method by giving an example of the signal event. A signal (background) event has a negative (positive) slope value. Figure 7.7 shows distributions of direction identification variables for two methods.

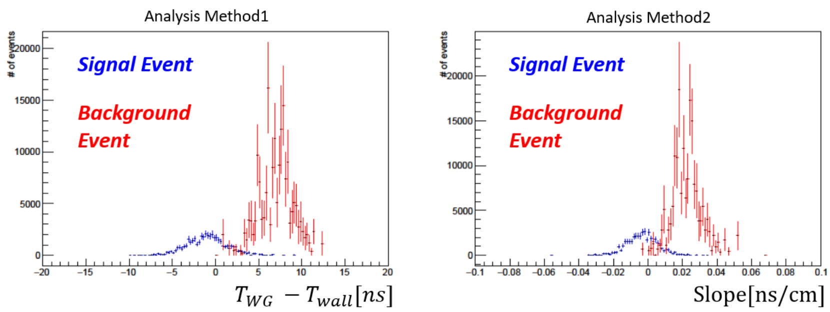

Figure 7.7: Direction identification variables for the two analysis methods (left: analysis method1, right: analysis method2). Blue (red) points with error bars correspond to the signal (background) events. Each entry was weighted by a factor to normalize the simulated data. The number of total entries corresponds to 1.084×10^{24} P.O.T.

7.2.2 Expected performance

Event efficiency

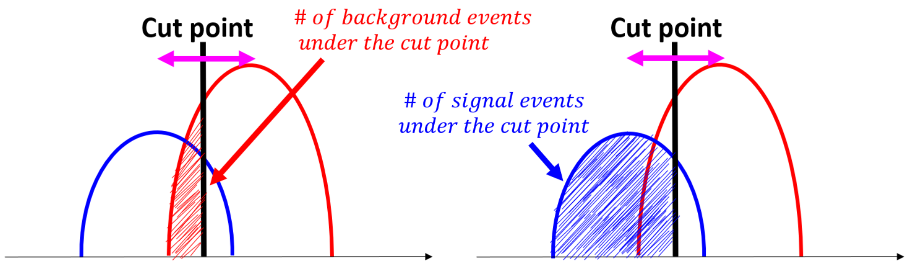

Figure 7.8: Definitions of the signal and background event efficiencies

In order to evaluate the background rejection capability, we caluculated the signal and background efficiencies using Figure 7.7. The definitions are as follows

$$\mathrm{Eff}_{\mathrm{signal}} \equiv \frac{\#\ of\ signal\ events\ under\ the\ cut\ point}{\#\ of\ total\ signal\ events} \tag{7.1}$$

$$\mathrm{Eff}_{\mathrm{background}} \equiv \frac{\#\ of\ background\ events\ under\ the\ cut\ point}{\#\ of\ total\ background\ events} \tag{7.2}$$

where, Eff is the defined efficiency. A cut point is set at a point in the histogram and the efficiencies are calculated as described in Figure 7.8. We scan the cut point in the whole region of the histogram and calculate them for each point. The correlations of the caluculated efficiencies for each method are fitted by inverse functions as shown in Figure 7.9.

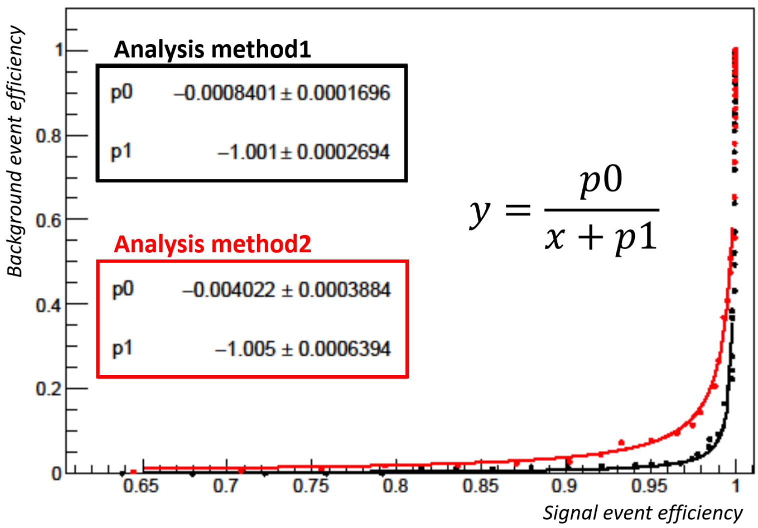

Figure 7.9: Correlations of the signal and background event efficiencies (black: analysis method1, red: analysis method2)

Expected background rejection

For a practical discussion, we use Table 7.1 and Figure 7.9. The number of background event is discussed assuming that we require the 95 % signal events corresponding to 177 events for 5.0×10^{21} POT. In this case, the background event efficiency of the analysis method1 is 0.016 and that of the analysis method2 is 0.073. They correspond to 13 events and 60 events respectively. Thus the analysis method1 can suppress the number of background event under 10% of the signal event. The values in this discussion are summarized in Table 7.2.

	Eff_{signal}	N_{signal}	$Eff_{background}$	$N_{background}$
Total	1.0	186	1.0	829
Method1	0.95	177	0.016	13
Method2	0.95	177	0.073	61

Table 7.2: Information of the variables for the discussion. N is the number of events. The results are assumed that we require the 95 % signal events corresponding to 177 events for 5.0×10^{21} POT.

7.3 Conclusion

The background from the south WallMRD to the downstream WAGASCI is found to be significant so that the background rejection is necessary. We have evaluated the background rejection capability using the Monte Carlo simulation. The analysis method1 and the analysis method2 were developed for the background event rejection. Assuming that we require the 95 % signal events corresponding to 177 events for 5.0×10^{21} POT, it was found that the analysis method1 has a potential to suppress the background events under 10% of the signal event.

Chapter 8

Summary

In order to reduce systematic errors on the T2K neutrino oscillation measurement, we study the neutrino-nucleus interaction at around 1 GeV by measuring the charged-current neutrino cross section ratio between H_2O and CH with a large phase space in the T2K-WAGASCI project. We have developed a neutrino detector named WAGASCI which enables the measurement of cross section on H_2O. Precise measurements are realized by the combination with a muon range detector(MRD) named WallMRD which tracks secondary particles from neutrino interactions. The preparation for the physics run and its beam measurement were described in this thesis.

A mass test of the 40 ASU boards for a WAGASCI detector was conducted at the University of Tokyo in April 2019. We checked performances for the MPPC gain tuning and the threshold curve measurement. In addition, we measured the TDC ramps to calibrate the difference.

In order to solve a problem with a timing measurement found in the second pilot run, we improved the DIF firmware. The time measurement system was synchronized to the external trigger by adding several functions to the firmware. The firmware enabled the reconstruction of the T2K neutrino beam bunch structure by hit timings.

We started the first physics run with two WAGASCI detectors and two WallMRD detectors in November 2019. We calibrated the timing measurement system of the WAGASCI detector using the beam data. The difference between ASUs and the time walk effect were calibrated. The calibration improved the timing resolution of the WAGASCI detector from 15ns to 6.0ns.

We discussed a performance with timing information. The background from the south WallMRD to the downstream WAGASCI is found to be significant so that the background rejection is necessary. We have evaluated the background rejection capability using the Monte Carlo simulation. A developed method for the background rejection has shown a potential to suppress the background under 10 % of the signal event even though the number of the background event is 4 times larger than that of the signal event.

Appendix A

TDC dead range

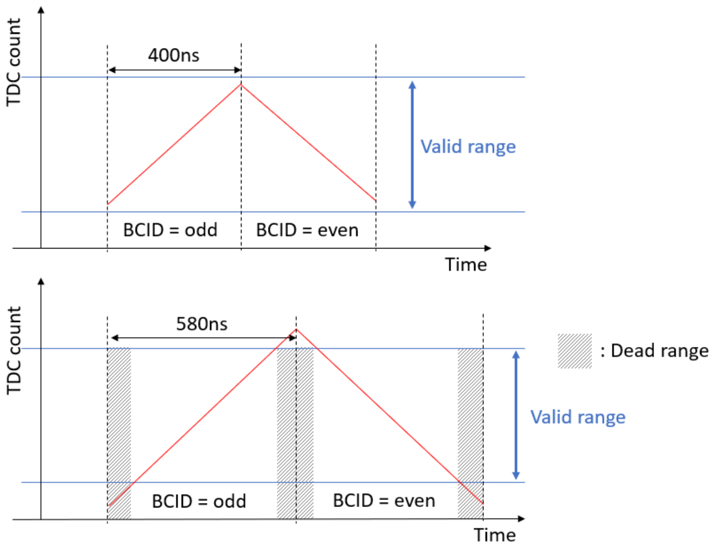

Figure A.1: TDC ramp in case that the period of the slow clock is 400ns(top). The period was changed to 580ns(bottom). Because the TDC ramp was designed for the slow clock with 400ns period, we have dead ranges.

TDC ramp is introduced in section 2.3.3. It is a ramp signal which gives us fine time information. The TDC ramp goes up when BCID is odd and goes down when BCID is even. The BCID is the number of the slow clock after the rising edge of the start-acq signal. The period of slow clock is 580ns, but it was 400ns originally. In order to optimize the timing system for the T2K beam bunch structure(Figure 1.3, right), we changed the period. Because the slope of TDC ramp is fixed, the ramp overflows or underflows the valid range of a 12-bit AD converter as shown in Figure A.1. Therefore we have dead ranges.

Appendix B

Timing tuning of the acquisition gate

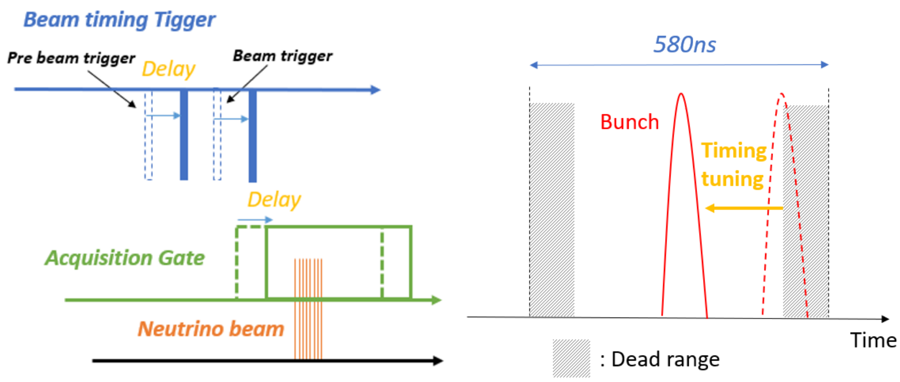

Figure B.1: Explanation of need of the timing tuning

We got an ability to observe the bunch structure of the T2K neutrino beam thanks to the improved DIF firmware(Chapter 4). As discribed in Appendix A, we have the dead ranges in the TDC. Thus, we needed to adjust the acquisition gate to match the beam timing to the valid TDC range as described in Figure B.1. For this purpose, we installed two NIM modules, a gate generator and a NIM-TTL converter. Their roles are as follows;

- Gate generator

  The acquisition gate is adjusted by delaying the beam trigger signal.(Figure B.2, left)

- NIM-TTL converter

  The (pre-)beam trigger signal is a NIM signal. CCC is activated by a TTL signal. Furthermore the CCC firmware and the improved DIF firmware were developed to detect a trailing edge. Therefore, we use the module which also works as an inverter. (Figure B.2, right)

The timing chart of signals is shown in Figure B.3. After the beam trigger is processed in the two modules, the signal is input to CCC and the start-acq signal is activated. The timing tuning worked well as show in Figure B.3.

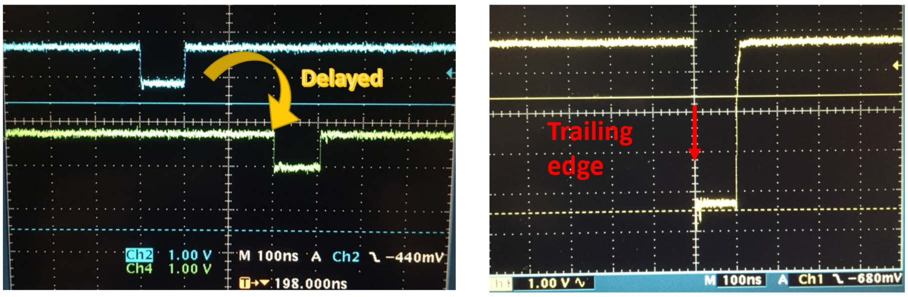

Figure B.2: Roles of the NIM modules (left: the gate generator, right: the NIM-TTL converter which works as an inverter.)

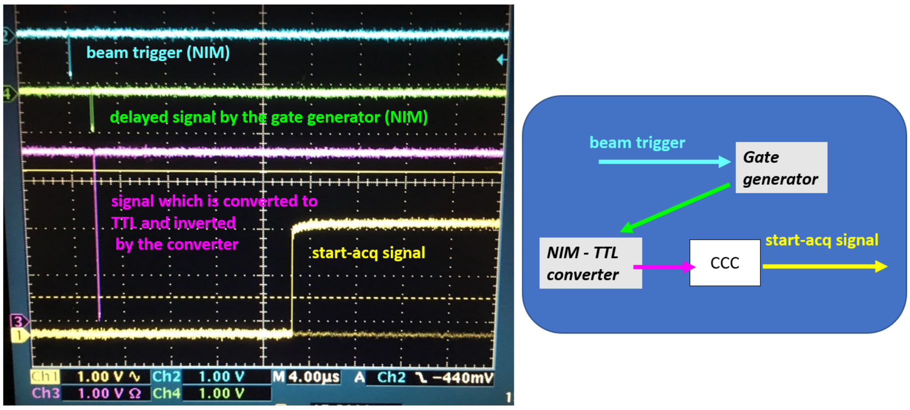

Figure B.3: Timing chart of signals

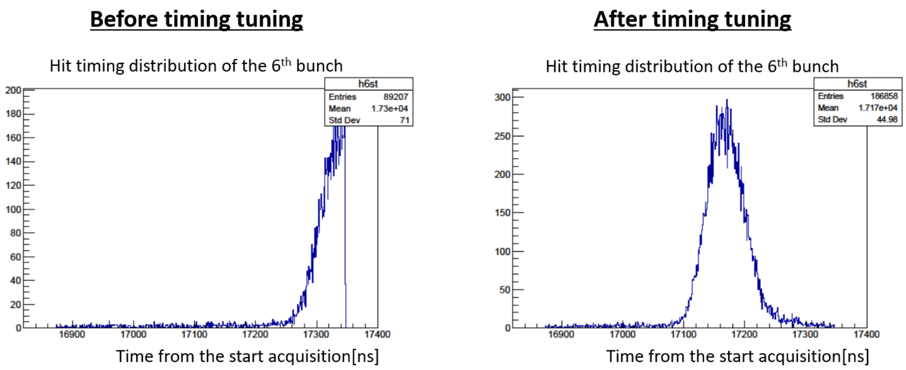

Figure B.4: Hit timing distribution of the sixth bunch of the neutrino beam (left: before timing tuning, right: after timing tuning)

Appendix C

Problem of the WallMRD electronics

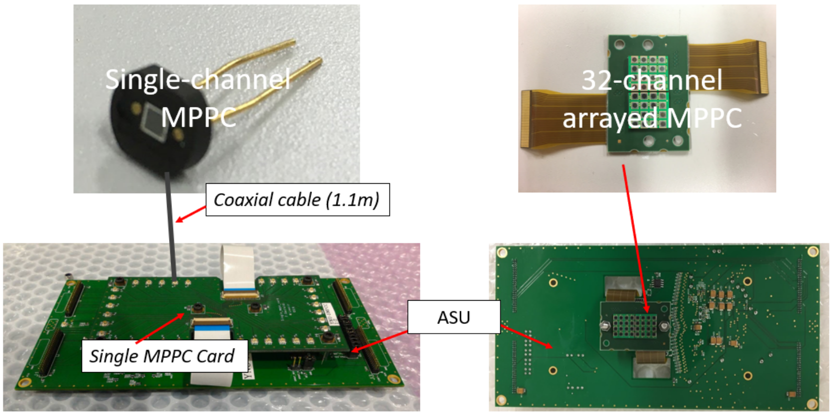

Figure C.1: Difference of readout system between WAGASCI and WallMRD. The 32-channel arrayed MPPC is used for the WAGASCI detector(right). The single-channel MPPC is used for the WallMRD detector. It is connected to ASU via the 110cm coaxial cable by the single MPPC card.(left)

The readout system of WallMRD causes problems which spoil the data taking of the physics run. As introduced in section 2.3.2, the single channel MPPC is applied for the WallMRD detector. We use the single MPPC card and the 110cm coaxial cable for the application. Regarding the readout system, the following problems were reported;

- Accurate hit timing is not recorded when ASUs are lined up in series.
- Large noise which is not removed by threshold of SPIROC2D.

On the other hand, we use the 32-channel arrayed MPPC for WAGASCI. The two problems were not reported in the case of the arrayed MPPC. The detail of the problems are explained in this chapter.

C.1 Delayed hit signal

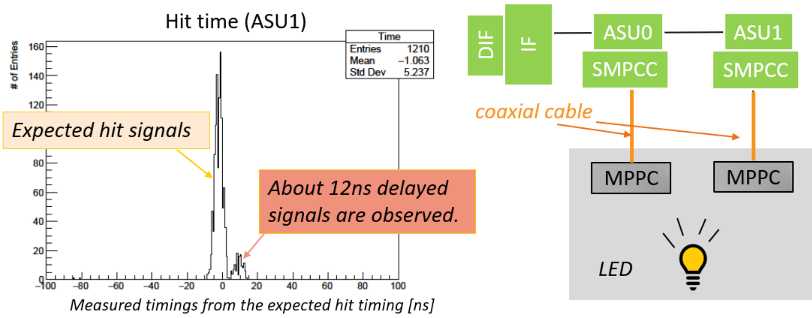

Figure C.2: Overview of the time resolution problem. We did a timing measurement with the right setup. A peak which is not that of the expected timing is shown in the left hit timing distribution.

This problem is caused when two or more ASUs are lined up in series. Some hit timings are delayed from the expected hit timing by about 12 ns as shown in Figure C.2(left). This plot was measured by injecting LED light to two single channel MPPCs which are connected to two single MPPC cards separately via the 110cm coaxial cables as shown in Figure C.2(right). The delayed signal was observed even though the light injection timing was synchronized to the start-acq signal.

The problem was not observed when we used short coaxial cables(20 cm). We guessed that the long coaxial cable acted like an antenna and thus collected some noise. Therefore we shielded the coaxial cable with aluminum foil and tested them as shown in Figure C.3. In addition, We eliminated the electric potential difference between the aluminum foil and the electronics boards. The result is shown in Figure C.4. The peak corresponding to the delayed signal is not shown. We wrapped all the 160 coaxial cables of the south WallMRD in aluminum foils and insulating tapes as shown in Figure C.5. We did not apply the shielded cables to the north WallMRD in order to investigate the other problem.

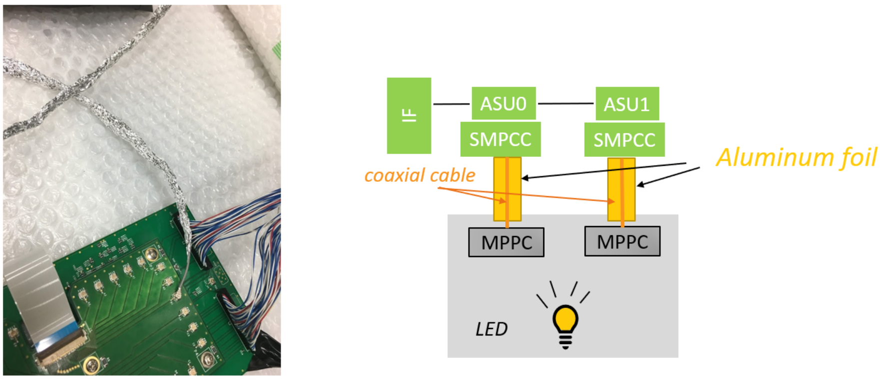

Figure C.3: Picture of the shielded cable(left) and test setup(right)

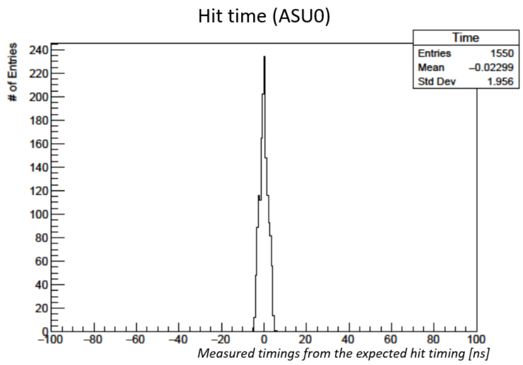

Figure C.4: Hit timing distribution of measurement with the shielded cables. Only the peak corresponding to the exepected timing is shown.

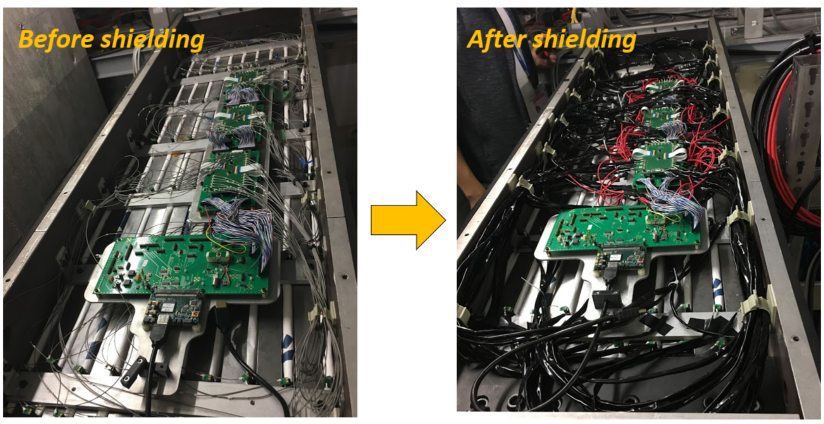

Figure C.5: Top view of the south WallMRD in the electronics box. We wrapped the coaxial cables in aluminum foils and insulating tapes. (left: before shielding, right: after shielding)

C.2 Noise problem

The WallMRDs had a problem due to a large noise as introduced in section 5.4. In the case of SPIROC2D, the acquisition is triggered when the signal is "below" the threshold. However we have noise which is not removed no matter where we set the threshold. It is found that the charge information corresponding to the noise hits is of the pedestal level. The noise is also observed in the laboratory. It decreased largely when we used short coaxial cables(20 cm). In addition, it also decreased by strengthening the ground connections between electronics boards. However we have not found solution by the end of 2019.

In order to estimate the effect of noise, we removed the noise by analysis. We can remove it by charge information. We checked that the noise was removed appropriately by a correlation between hit timing and charge. The WallMRD has two readouts at the top side and the bottom side. If a hit position is near the readout of top side, the charge of top side should be larger than that of bottom side. Furthermore, the recorded hit timing of top side should be earlier than that of bottom side. The same applies the case that the hit position is near the readout of bottom side. The expected correlation is explained in Figure C.6.

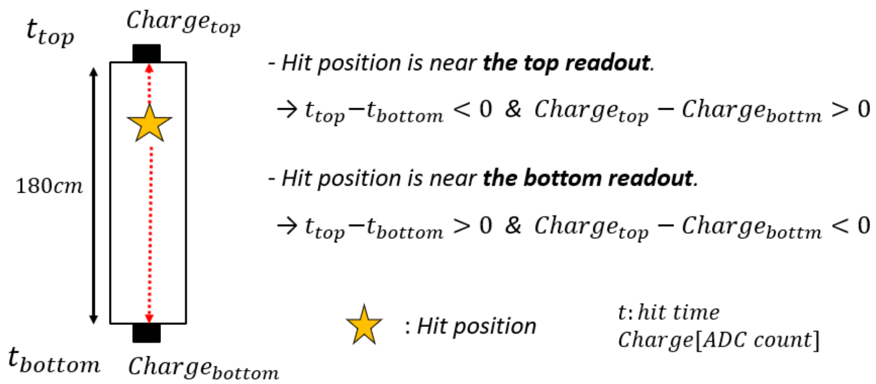

Figure C.6: Expected correlation between hit timing and charge.

Figure C.7 shows the correlations we checked. The beam data of the south WallMRD with 273288 spills was analyzed. The time clustering which is introduced in section 6.2 was applied. We requested three or more hits to start clustering for each side. After the clustering, we checked hit channel matching between the top side and the bottom side. We selected the event when the number of the matched channel was three or more. In order to remove the noise, we imposed a condition that charge is not pedestal. The left histogram is the result of the case that we did not remove the noise. The distribution includes many entries which do not have the correlation we expected. Furthermore the noise concentrates on the uppper right area in the histogram except for the area in which the charge difference is close to zero. That indicates that the noise of bottom side is more serious than that of top side. The right histogram is the result of the case that we removed the noise by analysis. The plot shows the correlation we expected. We can estimate the effect of noise by comparing the two results. The left histogram consists of 32161 events and the right consists of 10758 events. The selected events decreased by 67%.

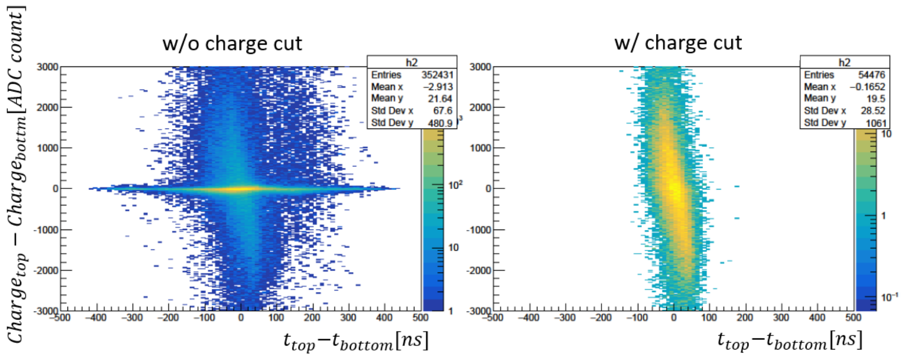

Figure C.7: Result of the noise reduction by analysis.(left: without charge cut, right: with charge cut).

Appendix D

Transportation time of the start-acq signal

DIF sends the start-acq signal to each ASU. After receiving it, ASUs open an acquisition gate. The opening time of each ASU should have a time lag due to the transportation time of the signal. In order to measure the time lag, a test setup was constructed as shown in Figure D.3(left). A single channel MPPC was injected by LED light which was synchronized to the start-acq signal. In order to remove an effect of individual ASUs, only one ASU was connected to the MPPC and the ASU was inserted between the lined-up ASUs one by one. The MPPC and the LED were fixed in the black box not to change the situation. The measured hit timing distributions of each case are shown in Figure D.3(right). The time lag per an ASU corresponds to approximately 3ns so that the effect can become up to 12 ns.

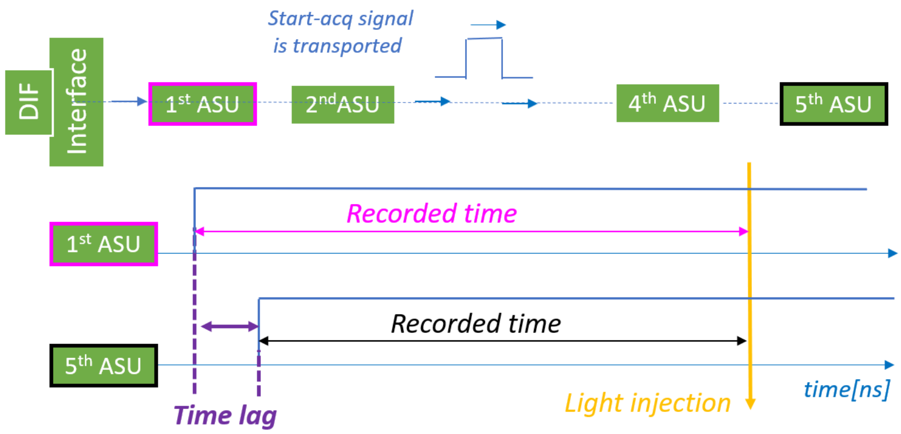

Figure D.1: Explanation of the time lag due to the transportation time of the start-acq signal.

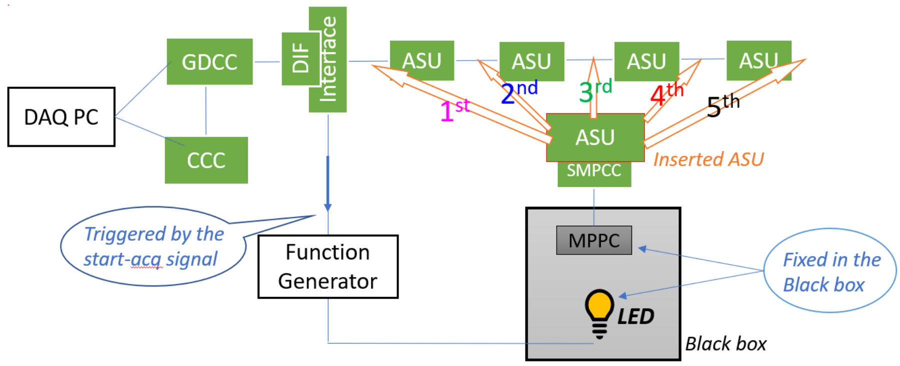

Figure D.2: Test setup to measure the delay due to the transportation time of the start-acq signal.

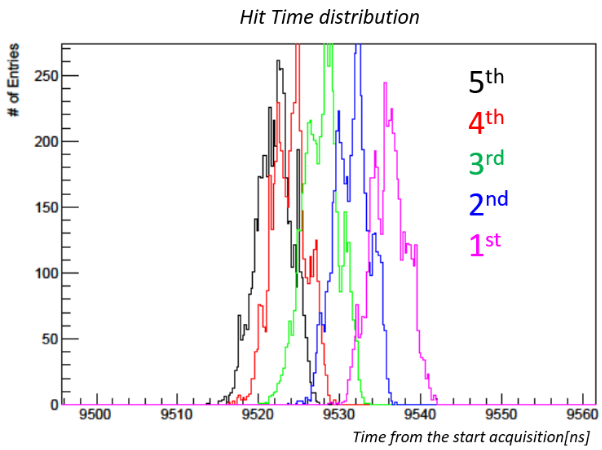

Figure D.3: Hit timing distribution of ASUs at each position.

Appendix E

Background rejection using the Michel electron

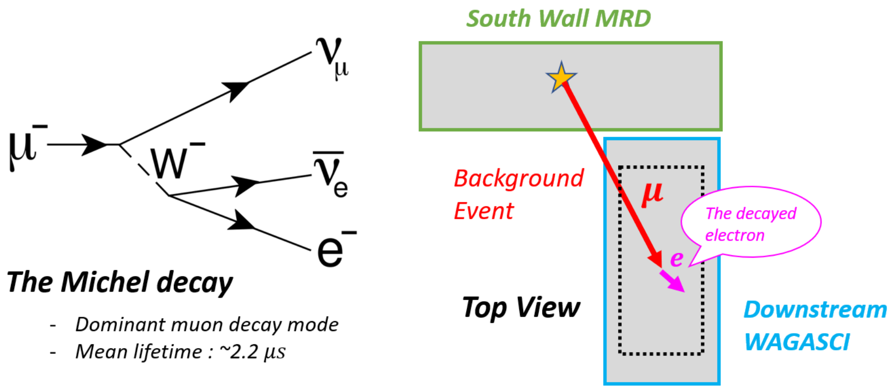

Figure E.1: Diagram of the Michel decay(left) and illustration of the background event in which the Michel electron is generated(right).

The background event discussed in Chapter 7 can be removed by detecting a track of the Michel electron. It does not need a high-quality timing performance.

We defined the background event that a neutrino interaction occurs in a WallMRD and the generated muon stops in WAGASCI. After the muon stoped in WAGASCI, it can decays to a electron as shown Figure E.1(left). This decay mode is called the Michel decay and it is a dominant decay mode. The mean life time is around 2.2 μs. When we found a event to distinguish the signal event and the background event, we can identify the background event by detecting a track of the Michel electron in WAGASCI as shown in Figure E.1(right). In order to detect the track, we should meet the following conditions.

- Large range enough to be recognized as a track.

  To identify a track of the Michel electron, it must have a large range to leave many hits.

- High frequency of the Michel event.

If the Michel event occurs rarely, the analysis to search the electron becomes a wasted effort.

- DAQ system to catch the delayed hit signal.

  Because of the life time, the hit timings by the electron are delayed from the hit timings of a neutrino interaction. We need an ability to catch the delayed hit signals.

We discuss whether our situation meets the conditions.

E.1 Range of the Michel electron

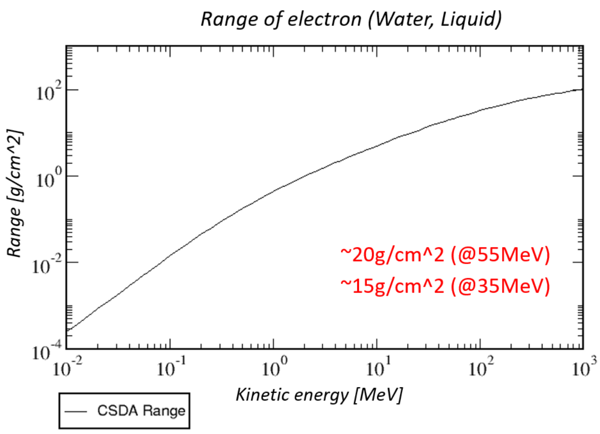

Figure E.2: Range of electron in water [24]

Figure E.2 shows electron's range in water as a funtion of its kinematic energy. Because the WAGASCI detector is filled by water and consists of thin scintillator bars(3mm), we checked the range in water. The maximun kinematic energy of the Michel electron is appropriately 55 MeV and the mean is appropriately 35 MeV. According to the graph, they correspond to $20g/cm^2$ and $15g/cm^2$ respectively. Because the density of water is $1.0g/cm^3$, the ranges of each case are $20cm$ and $15cm$. On the other hand, the gap between channels of WAGASCI is $2.5cm$ so that the Michel electron can leave 6 hits on average or up to 8 hits. The hit numbers are enough to identify the track.

E.2 Frequency of the Michel event

We discuss the case of neutrino beam. The muons generated from neutrino interactions are negative ones (μ^-). The lifetime of negative muon is affected by not only the Michel decay but also the nuclear capture because of its electric charge. Table E.1 shows the lifetime of decay and nuclear capture and the total lifetime of negative muons in different materials. The fiducial volme of the WAGASCI module consists of hydrogen, carbon, and oxygen and the capture lifetime is larger than the decay lifetime in each case. That indicates that negative muons which stops in the WAGASCI module often decay by the Michel mode. Therefore we can count on many events of the Michel decay. In the case of anti-neutrino beam, we do not have to consider the nuclear capture.

Material	Atomic number	Decay	Capture	Total
Hydrogen	1	$2.2\mu s$	$2.4 \times 10^3 \mu s$	$2.2\mu s$
Carbon	6	$2.2\mu s$	$25\mu s$	$2.0\mu s$
Oxygen	8	$2.2\mu s$	$10\mu s$	$1.8\mu s$
Iron	26	$2.2\mu s$	$0.22\mu s$	$0.2\mu s$

Table E.1: The lifetime of decay, that of nuclear capture and the total lifetime of negative muons in different materials.

E.3 DAQ system

As introduced in section 2.3.3, SPIROC has an analog memory array with a depth of 16 for each is used to store the time information and the charge measurement. It enables the detection of the delayed signal of the Michel electron.

E.4 Conclusion

From the above discussions, our situation meets the conditions to utilize the Michel electrons for the background removal. We should develop the track reconstruction algorithm for the Michel electrons.

Acknowlegments

First of all, I would like to offer my special thanks to my supervisor, Masashi Yokoyama. His advices always helped my reserch and led my idea in the right direction. I could not complete this thesis without his help. In addition, he gave me the best environment which made me absorbed in my reserch. I met great members there. I want to express my gratitude to them: Aihara-san, Onuki-san, Iwamoto-san, Koga-san, Jin, Chikuma-san, Niikura-san, Alejandro, Wan, Fujita-san, Tang, Zhang, Ogawa-san, Kikutani-kun, Eguchi-kun, Yoshimoto-san. I could enjoy my life at the University of Tokyo thanks to them.

I would like to thank the T2K-WAGASCI convenors: Akihiro Minamino, Tatuya Kikawa and Etam Noah. I would like to thank Franck Gastaldi, Thomas Mueller and Stephane Callier for technical assistance of the WAGASCI electronics. I would like to thank Kenji Yasutome for technical assistance of the Monte Carlo simulation for the T2K-WAGASCI project. I would like to thank members working together at J-PARC: Ken'ichi Kin, Giorgio Pintaudi, Ngoc Tran, Naoya Kukita, Shin'ya Tanaka, Yuki Asada, Takuya Kobata, Takashi Honjo and Yuna Katayama.

Finally, I would like to show my greatest appreciation to my parents.

List of Figures

List of Tables

Bibliography

[1] P. I. Krastev and S. T. Petcov, Phys. Lett. B 205, 84 (1988).

[2] C. Jarlskog, Z. Phys. C 29, 491 (1985).

[3] Yoshinari Hayato, Seminar of neutrino interaction with nucleus and their simulation, http://www-he.scphys.kyoto-u.ac.jp/nufrontier/
les/hayato- 20140111.pdf

[4] K.Abe *et al.*(T2K collaboration), “Measurement of the T2K neutrino beam properties using the INGRID on-axis near detector”,Nucl. Instrum. Meth. A 694 211(2012)

[5] S. Assylbekov *et al.*, “The T2K ND280 Off-Axis Pi-Zero Detector”, Nucl. Instrum. Meth. A 686 48 (2012)

[6] N. Abgrall *et al.*, “Time Projection Chambers for the T2K Near Detectors”, Nucl. Instrum. Meth. A 637 25 (2011)

[7] P. A. Amaudruz *et al.*, “The T2K Fine-Grained Detectors”, Nucl. Instrum. Meth. A 6961 (2012)

[8] D. Allan *et al.*, “The electromagnetic calorimeter for the T2K near detector ND280”, Journal of Instrum. 8 10019 (2013)

[9] S. Aoki *et al.*, “The T2K Side Muon Range Detector (SMRD)”, Nucl. Instrum. Meth. A 698 135 (2013)

[10] Y. Fukuda *et al.*(Super-Kamiokande Collaboration), “The Super-Kamiokande detector”, Nucl. Instrum. Meth. A 501 418 (2003)

[11] T. Koga *et al.*, “Water/CH Neutrino Cross Section Measurement at J-PARC (WAGASCI Experiment)”, JPS Conf. Proc. **8**, 023003 (2015).

[12] K. Nitta *et al.*, “The k2k scibar detector”, Nucl. Instrum. Meth. A, 535:147, 2004.

[13] K.Yasutome, 新検出器 Baby MIND を導入した T2K-WAGASCI 実験の最適化と解析アルゴリズムの構築, Master’s thesis, Kyoto University (2019).

[14] N. Chikuma *et al.*, “Development of electronics and data acquisition system for the J-PARC T59(WAGASCI) experiment”, PoS EPS-HEP2017, 780 (2017).

[15] F. Gastaldi, R. Cornat, F. Magniette and V. Boudry, “A scalable gigabit data acquisition system for calorimeters for linear collider”, PoS TIPP **2014**, 193 (2014).

[16] Omega, SPIROC 2 User Guide(2009).

[17] K. Abe *et al.* [T2K Collaboration], “Measurement of the ν_μ charged-current cross sections on water, hydrocarbon, iron, and their ratios with the T2K on-axis detectors,” Prog Theor Exp Phys (2019)

[18] T. Koga, “Measurements of neutrino interactions on water and search for electron anti-neutrino appearance in the T2K experiment”, Doctorate Dissertation, The University of Tokyo(2018)

[19] N. Chikuma, “Measurements of neutrino charged-current interactions on water and hydrocarbon targets using a sub-GeV anti-neutrino beam”, Doctorate Dissertation, The University of Tokyo(2019)

[20] K.Okamoto, J-PARC WAGASCI プロジェクトの横方向ミューオン検出器用シンチレータの性能評価, 日本物理学会 2018 年次大会

[21] K.Abe *et al.*, [T2K collaboration], T2K neutrino flux prediction, Phys.Rev. D87 (2013) no.1, 012001

[22] Y.Hayato, “NEUT” , Nucl. Phys. Proc. Suppl. 112, 171 (2002)

[23] R.Brun *et al.*, “GEANT-Detector Description and Simulation Tool” Cern Program Library Long Write-up W5013 (1993)

[24] NIST (USA). Stopping-Power and Range Tables for Electrons, Protons, and Helium Ions. http://www.nist.gov/pml/data/star/index.cfm.